Comparative study of hot-wire and multi-hole pressure probe performance in low-Reynolds-number turbulent flows

Simon Dehareng[1*], Thomas Gemine[2], Geoffroy Lumay[2], Thomas Andrianne[1]

[1]Department of Aerospace and Mechanical Engineering, University of Liège, 4000, Liège, Belgium.
[2]GRASP Laboratory, University of Liège, 4000, Liège, Belgium.

*Corresponding author. E-mail: Simon.Dehareng@uliege.be;

Abstract

This study investigated the performance of hot-wire anemometry and a multi-hole Cobra pressure probe for turbulence characterization in a small-scale, 3D-printed wind tunnel operating at a Reynolds number of $\mathbf{2.6 \times 10^4}$. Experiments were conducted under passive grid-generated turbulent conditions, resulting in freestream turbulence (FST) levels of **2%**, **4%**, and **8%**. Despite the Cobra's practical advantages (robust, geometry-dependent pre-calibration and simultaneous three-component velocity measurements), it showed limitations due to a restricted sampling frequency and the probe's head geometry, leading to spectral deviation and biased turbulence estimates. Post-processing strategies were devised to mitigate these effects. A second-order polynomial spectral correction improved estimates of RMS fluctuations and the integral length scale ($\boldsymbol{L}$). At the same time, an approach based on equilibrium dissipation laws enabled consistent estimation of dissipation-related quantities, including the Taylor microscale ($\boldsymbol{\lambda}$), Kolmogorov scale ($\boldsymbol{\eta}$), and dissipation rate (ε), without relying on velocity gradients, which are highly dependent on the pressure probe's limitations. Validation in a large-scale wind tunnel confirmed that corrected Cobra-based dissipation estimates could achieve relative errors below **30%** compared with hot-wire data. Overall, the results demonstrate that, when combined with the proposed corrections, the Cobra probe can provide a good estimate of turbulence features despite its intrinsic frequency limitations, offering a practical alternative to hot-wire anemometry in low-Reynolds-number turbulent flows.

Keywords: keyword1, Keyword2, Keyword3, Keyword4

1 Introduction

The characterization of turbulent flows in wind tunnels is a fundamental challenge in experimental aerodynamics. The study of turbulence statistics is crucial due to its now widely acknowledged influence in most real-world applications: bluff-body aerodynamics (Lee, 1975; Bearman and Morel, 1983), wing efficiency (Bailey et al., 2006; Watkins et al., 2010), and fluid-particle interaction (Sumer et al., 2003; Creyssels et al., 2009; Valance et al., 2015). Characterizing velocity fluctuations along with turbulence structures at various scales is essential for modeling and understanding the impacts of turbulence in such applications.

Among the most commonly used measurement tools are the multi-hole probe (also called Cobra probes) and the hot-wire anemometry. The Cobra probe enables straightforward and rapid measurements of the three instantaneous velocity components, $u(t)$, $v(t)$, and $w(t)$, as well as insights into large-scale flow structure. In contrast, hot-wire anemometry, while capable of capturing high-frequency signals and resolving the smallest flow scales, typically measures only one velocity component in its simpler configuration (single wire). Three velocity components are accessible, but after a cumbersome calibration procedure. Additionally, it requires more complex and delicate setups and is more prone to breaking under harsh flow conditions.

The use of hot-wire anemometry for turbulent flow characterization is well-established and widely documented (Comte-Bellot, 1976; Jørgensen, 2001). In contrast, pressure-based probes are generally used for the identification of large-scale anisotropies, given their limited frequency resolution. Hooper and Musgrove (1997) showed that a four-hole Cobra probe could accurately measure, with quantified uncertainties, all components of the Reynolds stresses as well as the mean velocity components in a fully developed turbulent pipe flow. While the results showed general agreement with key turbulence statistics, they reported a 20% overestimation of streamwise velocity fluctuations and a 20% underestimation of transverse fluctuating components compared to hot-wire measurements. According to these authors, these discrepancies were attributed to an insufficient sampling rate and pressure tubing limitations. More generally, the performance of a pressure probe is constrained by two primary sources of error:

- Spatial limitations: The probe's physical dimensions and the spacing of its pressure taps have a direct influence on the probe's performance. These effects were highlighted by Moss and Oldfield (1990), who identified the probe diameter-to-wavelength ratio as a key factor influencing the measured energy spectra beyond a certain frequency, when comparing hot-wire anemometry and fast-response pressure transducers in hostile flow conditions. Later, Heckmeier et al. (2021), when investigating the spatial and temporal resolution of a pressure probe in a turbulent flow generated by a grid ($Re_M = [4300; 12800]$ with $M = 6.4$ mm, the grid mesh size), confirmed that its performance is fundamentally limited by its physical dimensions.
- Frequency limitations: The pressure tubing acts as an acoustic filter. (Moss and Oldfield, 1990) also pointed to resonance phenomena within the tubing system as a source of the measurement difference between the hot-wire and pressure probe.

Despite these critical limitations, pressure probes have shown a lot of potential. Chen et al. (2000) compared the main statistics obtained with a Cobra probe in a developed pipe flow with hot-wire data at $Re_{D_h} = 1.0 \times 10^5$ and at a FST lower than 2.5%. The results showed good agreement between the two measurement systems, suggesting that the Cobra probe could actually capture a broad range of flow characteristics. Obligado et al. (2022) conducted an experimental study in a wind tunnel for a turbulent boundary layer with a FST lower than 0.2% and Reynolds numbers in the range of $Re_{D_h} \in [1.7; 5.9] \times 10^5$, using a combination of single-wire anemometry and a Cobra probe. They compared the experimental results with the ones of direct numerical simulations to assess the turbulence scales of the flow and the dissipation rate, ε. They concluded that the combined use of both instruments compensates for the Cobra probe's limited frequency resolution at smaller scales, while providing complementary information on turbulence anisotropy, which is not offered by the simple hot-wire.

This study aims to extend previous literature on turbulent flow characterization by evaluating the potential of the Cobra probe as a standalone measurement device. The objective is to simplify turbulence measurements in low- and moderate-Reynolds-number configurations by relying solely on the Cobra probe, which offers the advantage of measuring all three velocity components and comes with a robust pre-calibration that depends only on the probe's geometry. This makes it unlikely to be affected by residual temperature effects or aging, while also avoiding the technical constraints and complexity associated with hot-wire anemometry, particularly in confined environments such as small wind tunnels. This approach responds to the initial motivation to overcome the practical difficulties encountered when setting up a hot-wire system in such constrained spaces. However, limitations such as the Cobra probe's restricted frequency response, the fixed, manufacturer-defined inverse transfer function, and the physical dimensions of the probe itself hindered full-spectrum turbulence characterization. This study, therefore, addresses these challenges through simple adapted post-processing methods and compares results with those obtained from hot-wire anemometry, ultimately assessing the feasibility of using only the Cobra probe for detailed turbulence analysis.

2 Experimental setup

2.1 Wind tunnel facility

The focus of this study was placed on low-to-moderate-Reynolds-number airflows. For this purpose, a small-scale, open-loop wind tunnel was designed and 3D-printed following design criteria from Mauro et al. (2017). The configuration used for the experiments features a square test section with dimensions of 68 mm × 68 mm × 450 mm in width, height, and length, respectively. This suction-type wind tunnel, shown in figure 1, is driven by a DC axial compact fan that can be throttled to reach the target freestream velocity. Additionally, static turbulence grids can be installed at the test-section inlet to increase the turbulence level. The origin of the coordinate system $[x, y, z]$ is located on the centerline at the inlet of the test section, as shown in the schematic figure 2. The x-, y-, and z-axes represent the streamwise, transverse, and vertical directions, respectively. The corresponding velocity components are represented by $[u, v, w]$. The

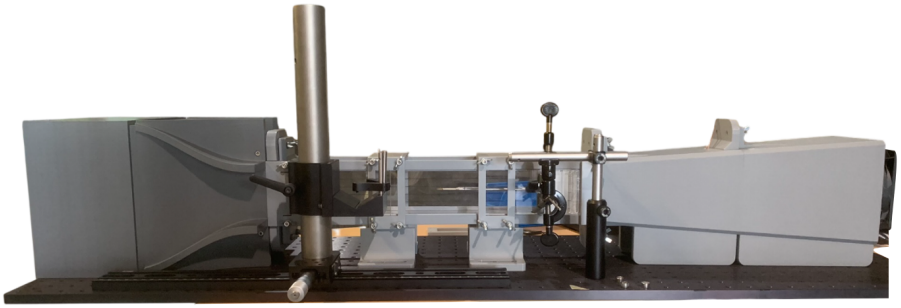

Fig. 1: Experimental setup.

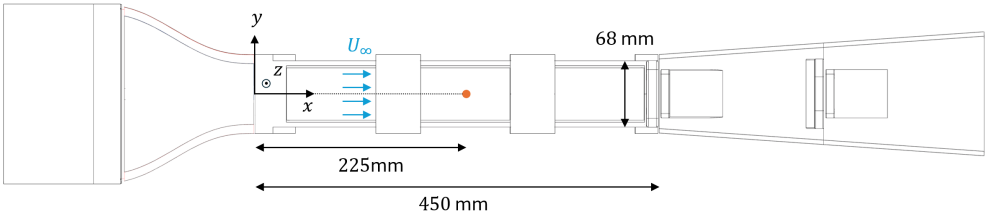

Fig. 2: Schematic top-view of the 3D-printed small-scale suction wind tunnel.

notations for the rest of the paper are as follows: $\overline{x}$ for time-averaged quantities, x' for the fluctuations, and $\langle x \rangle$ for an ensemble average of quantity x.

2.2 Turbulence grids

The quantities reported in the present study were measured at a freestream velocity of $U_\infty \approx 5.7$ m/s. This corresponded to a hydraulic-diameter-based Reynolds number $Re_{D_h} = 2.6 \times 10^4$. Four distinct turbulence conditions were investigated. The first case, REF, served as a reference for establishing baseline conditions in a clean test section. The convergent section (0.18 m $\times$ 0.18 m in height and width), the honeycomb, and a fine grid screen ensured a turbulence level below 0.5 %. The turbulence intensity in the present manuscript is defined as $T_i = \sqrt{\overline{u'^2}}/\overline{u}$, with u' represented as $u' = u(t) - \overline{u}$ (where $u(t)$ is the instantaneous velocity and $\overline{u}$ is the time-averaged velocity). Turbulence was generated at different levels using passive grids for three other cases, A, B, and C. The design of the passive grids for the generation of turbulence was based on the methodology in Vita et al. (2018). Letting b be the width of the bars and M the mesh size, the grids were designed to keep a grid porosity $\beta = (1 - b/M)^2$ of more than 50 % to prevent large-scale instabilities in the wake (Kurian and Fransson, 2009; Ertunç et al., 2010). The grid geometrical properties are reported in table 1.

Table 1: Summary of the passive grids characteristics.

Grid case	b (mm)	M (mm)	x/M	β
A	1.20	5.32	42.29	0.6
B	3.20	14.20	15.84	0.6
C	5.52	24.50	9.18	0.6

2.3 Measurement devices

The measurements were taken on the centerline at mid-length of the test section ($x/D_h = 3.31$) using a Cobra probe manufactured by *Turbulent Flow Instrumentation* (Series 100). The head of the probe, shown with its dimensions in figure 3(a), is equipped with four 0.5 mm pressure taps connected via tubing to pressure transducers located within the probe body. A central pressure tap is positioned on a plane perpendicular to the flow, while three additional taps are arranged circumferentially around the central one, spaced at 120° intervals. These taps are mounted on planes oriented to define an acceptance cone of ±45° with respect to the probe's x-axis. The conversion of measured pressures into velocity components is achieved using a steady-state calibration approach, originally proposed by Shepherd (1981) and adapted for the Cobra probe by Hooper and Musgrove (1997). For each yaw and pitch angle during calibration, the minimum pressure among the three outer taps is designated as P_k, while the other two are labeled P_i and P_j through cyclic selection. Together with the central pressure P_0, these pressures form the non-dimensional ratios

$$X_1 = \frac{P_i - P_j}{P_0 - P_k}, \qquad X_2 = \frac{P_j - P_k}{P_0 - P_k}, \qquad X_d = \frac{0.5\rho U_\infty^2}{P_0 - P_k}, \qquad X_t = \frac{P_t - P_0}{P_0 - P_k}. \tag{1}$$

The ratios X_1 and X_2 calculated directly from the instantaneous pressure readings act as the independent variables for constructing four calibration surfaces that represent the dependent quantities: yaw angle, pitch angle, dynamic pressure ratio X_d, and total pressure ratio X_t. During post-processing, the instantaneous pressures from the four taps are matched to these pre-established calibration surfaces through look-up tables generated from the factory calibration. The angular measurement accuracy is ±1°. According to the manufacturer's specifications, the probe was calibrated to operate in flow velocities ranging from 2 to 55 m/s, with a velocity measurement accuracy of ±0.3 m/s. This multi-hole pressure probe, designed primarily to capture the large-scale flow structures and to provide information on the three components of the flow, has a recommended maximum sampling frequency f_s of 2000 Hz. A preliminary study on the influence of f_s on the turbulence spectrum demonstrated that increasing this frequency up to 2500 Hz was acceptable. The acquisition frequency, f_a, was set to 16 times f_s to reduce measurement noise at higher frequencies. Data were acquired for 120 s, which was sufficiently long to converge to the mean freestream velocity and turbulence intensity.

Hot-wire (HW) anemometry was performed using the straight fiber-film x-probe *55R51* from *Dantec*. This probe consists of two quartz fibers, each 70 μm in diameter and 3 mm in length, arranged in an X-array configuration where they are oriented

at 90° relative to each other. The probe and its dimensions are shown in figure 3(b). Overall, the projected area for each instrument in the wind tunnel represented less than 2% of the test section area, which was considered acceptable. The measurements were performed at the same location (shown by the orange dot in figure 2) for both the HW and the Cobra probe. Figure 3(c) shows an upstream view of the section through a static turbulence grid. Both acquisition and calibration were performed using the *Dantec StreamLine* constant temperature anemometer. Data acquisition was carried out at a sampling frequency f_s of 50 kHz to ensure that all flow scales could be captured for a duration of 120 s. The signal was filtered to remove any potential high-frequency noise to keep only the relevant scales of the flow. This process involved data filtering using a seventh-order low-pass Butterworth filter applied at the Kolmogorov advection frequency, $f_K \sim \overline{u}/(2\pi\eta)$, where η [m] represents the Kolmogorov dissipation scale. This frequency was determined through an iterative procedure: Initially, a cutoff frequency of $f_c = f_s/2.5$ was chosen to provide a preliminary estimate of the Kolmogorov dissipation scale, calculated using spatial velocity gradients as follows:

$$\eta = \frac{\nu^{3/4}}{\varepsilon^{1/4}} = \frac{\nu^{3/4}}{\left[15\nu \left\langle \left(\frac{\mathrm{d}u}{\mathrm{d}x}\right)^2 \right\rangle\right]^{1/4}}, \tag{2}$$

where ε [$\mathrm{m^2 s^{-3}}$] is the dissipation rate, ν [$\mathrm{m^2 s^{-1}}$] is the kinematic viscosity, and $\mathrm{d}x = \overline{u}\mathrm{d}t = \overline{u}/f_s$ is a spatial increment obtained through Taylor's frozen turbulence hypothesis for one-point statistics (Taylor, 1938). The corresponding advection frequency f_K was derived and compared with the initial f_c using this characteristic length scale. This was repeated iteratively until the process converged to a stable value. Equation 2 is only valid in the case of Homogeneous and Isotropic Turbulence (HIT). To verify the validity of these assumptions within the context of this study, the characterization of the grid-generated turbulent flow was carried out in the test section. Details about the flow homogeneity are presented in appendix A.

The probes were positioned with an uncertainty of approximately 1 mm using a positioning plate specifically designed for this purpose. Regarding temperature control, a maximum variation of 0.5°C was allowed before repeating the calibration for the HW. Following the uncertainty analysis presented in Benedict and Gould (1996), the maximum random errors in the turbulence intensity measurement for the Cobra probe and the HW were less than 0.5 %.

The mean velocities, the root-mean-square of the fluctuations (RMS), the turbulence intensity, and the isotropy ratios measured by the Cobra and HW anemometry at the mid-length of the test section are summarized in table 2. The streamwise fluctuations measured with the Cobra probe were systematically higher than those measured with the HW. The velocity uncertainty of 0.3 m/s specified by the manufacturer for the Cobra probe may contribute to this discrepancy, particularly in low-turbulence conditions where the RMS fluctuations fall below this threshold. The discrepancy, however, manifested as a consistent overestimation across all turbulence cases, with the maximum difference between the fluctuations measured by the hot-wire and those obtained with the Cobra probe remaining on the order of 30%. This suggests that

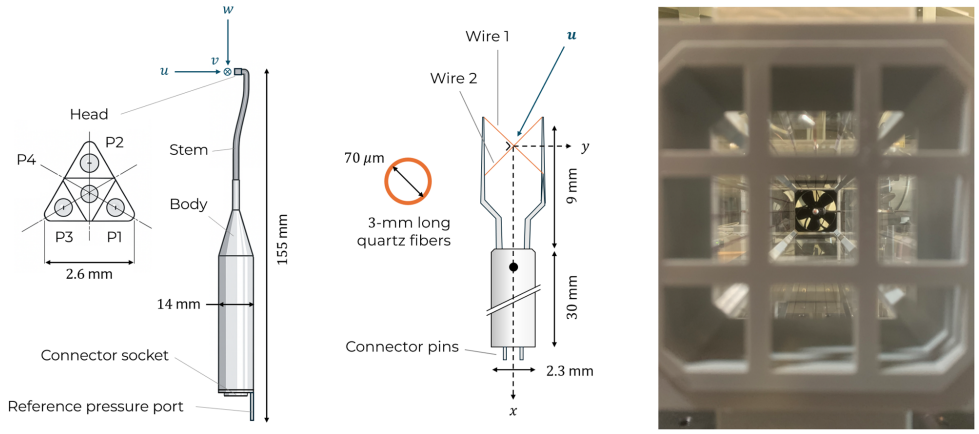

(a) (b) (c)

Fig. 3: Schematic diagram of (a) the Series 100 Cobra probe (adapted from Turbulent Flow Instrumentation website), (b) the X-wire probe 55R51 from *Dantec* (adapted from Jørgensen (2001)). (c) View through a turbulence grid from the inlet of the test section.

Table 2: Turbulence characteristics measured on the centerline at mid-length of the test section from both the HW and Cobra probe.

		Hot-Wire				Cobra Probe			
		REF	A	B	C	REF	A	B	C
$\overline{u}$	(ms^{-1})	5.98	5.64	5.65	5.68	6.03	5.76	5.83	5.86
Re_M	(−)	–	2000	5349	9277	–	2043	5519	9571
$\sqrt{\overline{u'^2}}$	(ms^{-1})	0.0217	0.1072	0.2430	0.4860	0.0289	0.1225	0.2767	0.5183
$\sqrt{\overline{v'^2}}$	(ms^{-1})	0.0225	0.1003	0.2483	0.4716	0.0168	0.0811	0.2044	0.3961
$\sqrt{\overline{w'^2}}$	(ms^{-1})	–	–	–	–	0.0149	0.0776	0.1981	0.3844
$\sqrt{\overline{u'^2}}/\overline{u}$	(%)	0.36	1.90	4.30	8.56	0.48	2.13	4.75	8.85
$\sqrt{\overline{u'^2}}/\sqrt{\overline{v'^2}}$	(−)	0.96	1.07	0.98	1.03	1.72	1.51	1.40	1.31
$\sqrt{\overline{u'^2}}/\sqrt{\overline{w'^2}}$	(−)	–	–	–	–	1.94	1.58	1.35	1.35

its origin lay elsewhere. This will be discussed in detail in the next section. The passive grids induced anisotropy consistent with what would be expected from Cobra probe measurements (Vita et al., 2018). The streamwise component measured with the Cobra appeared high compared to the transverse components for all cases. This will be subject to discussion in the next sections. This was not the case for the RMS fluctuations measured with the HW, which showed a reasonable isotropic turbulence field generally expected at such distances behind the grids (Isaza et al., 2014).

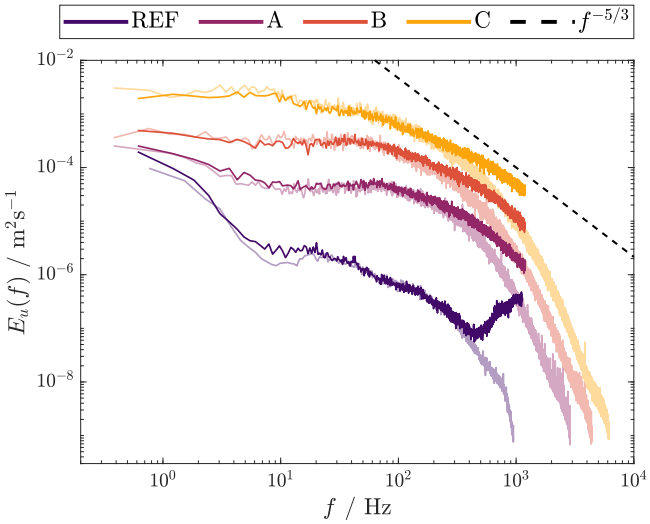

Fig. 4: Energy spectra in dimensional frequency space for all turbulence cases. The REF case is only plotted here for completeness. The opaque curves represent the spectra measured with the Cobra probe, while the transparent ones are from hot-wire measurements. The $-5/3$ law was added for reference.

3 Pressure probe limitations

The dimensional turbulent energy spectra obtained from the HW and Cobra probe timeseries are shown in figure 4. These were partitioned into 2^{11} and 2^{15} frequency bins, respectively, within which the values were then averaged. Firstly, the three expected turbulence regions appeared in the spectra measured with the HW (represented by the transparent curves): the energy-containing range represented by a plateau at low frequencies, the inertial subrange represented by the $f^{-5/3}$ law at moderate frequencies, and the dissipation range at higher frequencies. After filtering according to the method explained in section 2.3, the HW signal encompassed only the relevant range of turbulence scales present in the flow. As the FST increased from the REF case to grid C, there was an upward shift of the spectra, indicating an increase in energy, as expected for higher fluctuations. Additionally, the spectra shifted to the right, indicating a delay in energy dissipation through heat and, consequently, a reduction in the Kolmogorov scale. It is expected that a non-dimensionalization with viscous units, once determined, will show a collapse of the spectra onto one another. This would highlight the expansion of the inertial range with FST, as observed in studies investigating the influence of turbulence on the spectral shape (Larssen and Devenport, 2011; Hearst and Lavoie, 2015).

The Cobra probe spectra (represented by the opaque curves) aligned relatively well with the HW spectra, particularly within the energy-containing range and the onset of the inertial range. However, the Cobra failed to capture the onset of the dissipation range. This phenomenon also appeared in the studies by Moss and Oldfield (1990) and

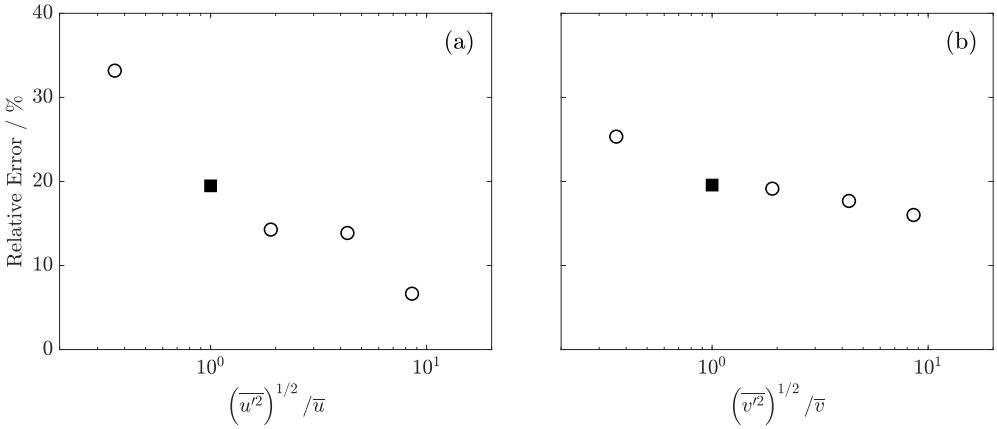

Fig. 5: Relative error of (a) RMS fluctuations in the streamwise velocity and (b) RMS fluctuations in the transverse velocity between Cobra and HW measurements. ■: Hooper and Musgrove (1997); ○: Present study.

Heckmeier et al. (2021). Given that the variance of a time series is obtained using

$$\overline{u'^2} = \int_0^\infty E_u(f)\mathrm{d}f, \tag{3}$$

it becomes evident why the streamwise fluctuations reported in table 2 were higher with the Cobra probe. Nevertheless, the reason for such a discrepancy remained somewhat unclear. As mentioned in the introduction, Hooper and Musgrove (1997) encountered a similar issue, namely discrepancies in the fluctuations measured with the Cobra probe. Specifically, they observed a 20 % overestimation of streamwise fluctuations and a 20 % underestimation of transverse fluctuations measured with the Cobra compared to the HW for a FST of 1 %. This outcome is compared with the results of the present study in figure 5, where a clear trend emerges showing better performance for the Cobra at higher FST. In Hooper and Musgrove (1997), the authors proposed two potential explanations for these discrepancies at low and moderate FST: signal undersampling and a poorly defined pressure transfer function.

The first potential cause arises from insufficient frequency resolution. This generates aliasing, leading to frequency-folding. This phenomenon is directly linked to the Nyquist-Shannon sampling theorem, which states that for a signal sampled at a frequency f_s,

$$B_w < f_s/2, \tag{4}$$

where B_w represents the bandwidth of the signal. Referring to figure 4 and considering that the HW captures the full range of scales of the flow, it is clear that the Cobra operated with a sampling frequency lower than two times the Kolmogorov advection frequency. Consequently, the signals measured by the Cobra were undersampled, leading to frequency folding. In this process, frequencies exceeding $f_s/2$ were folded back into the lower-frequency range. As a result, the loss of information due to undersampling had to be counterbalanced by a nonphysical increase in energy contributions

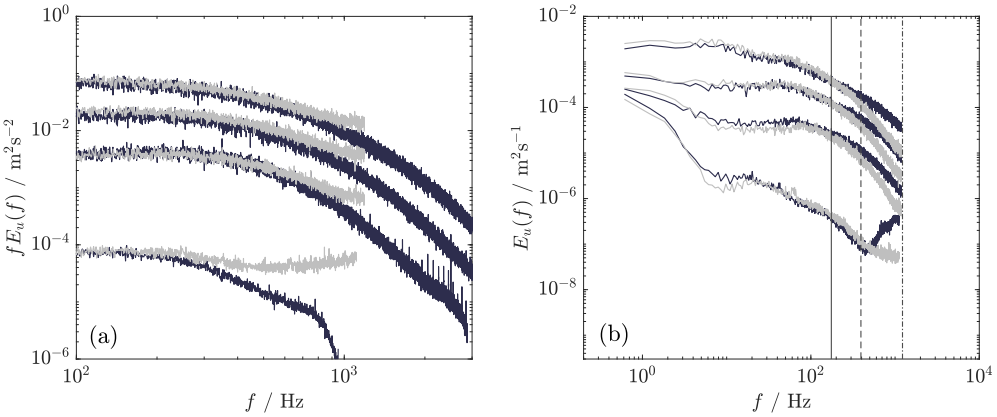

Fig. 6: Energy spectra in frequency space for cases REF, A, B, and C from bottom to top, respectively. (a) Comparison of HW well-sampled energy spectra, $E_u^{\mathrm{ws}}(f)$ (dark gray curve, $f_s = 50$ kHz), and HW undersampled energy spectra, $E_u^{\mathrm{a}}(f)$ (light gray curve, $f_s = 2.5$ kHz). The deviation between these spectra highlights the effect of aliasing on the hot-wire timeseries. (b) Comparison of Cobra energy spectra, $E_u^{\mathrm{c}}(f)$ (dark gray curve, $f_s = 2.5$ kHz), and HW undersampled energy spectra, $E_u^{\mathrm{a}}(f)$ (light gray curve, $f_s = 2.5$ kHz). −: f_{head}; - - -: f_{tap}; - · -: f_{tube}.

near $f_s/2$, ultimately contributing to some divergence between the spectra. Figure 6(a) compares the well-sampled spectra ($E_u^{\mathrm{ws}}(f)$, $f_s = 50$ kHz) to HW undersampled spectra ($E_u^{\mathrm{a}}(f)$, $f_s = 2.5$ kHz). The deviation between the two curves becomes apparent at high frequency. This observation confirms that aliasing, as expected, introduced a minor but discernible difference in the HW spectra from well-sampled and undersampled data. Next, figure 6(b) compares the aliased HW spectra ($E_u^{\mathrm{a}}(f)$, $f_s = 2.5$ kHz) to the Cobra probe spectra ($E_u^{\mathrm{c}}(f)$, $f_s = 2.5$ kHz). Both datasets were subjected to aliasing. The substantial difference between these two spectra suggests that factors other than aliasing must be responsible for the significant discrepancy. This implies that probe-specific characteristics or other measurement-related factors played a more significant role in the overall spectral deviation.

As a four-hole pressure probe, the Cobra is subject to two distinct, yet interconnected, limitations that could alter the signal reaching the pressure transducer: frequency limitations due to its tubing system and spatial limitations related to its probe head geometry (Hooper and Musgrove, 1997). First, the pressure tubes connecting the probe head to the transducers act as acoustic filters, attenuating high-frequency pressure fluctuations. These tubes can introduce amplitude and phase distortions that can significantly affect the output pressure signal, depending on their length and diameter (Kovaerk et al., 2018). This issue has been extensively investigated and characterized (Irwin et al., 1979; Hooper and Musgrove, 1997; Chen et al., 2000). To mitigate these effects, an inverse transfer function (determined experimentally by the manufacturer) is applied to the input signal, eliminating distortion and achieving a linear response up to frequencies exceeding 2000 Hz. For completeness, the system

transfer function was reassessed experimentally by exciting the system with a constant-amplitude sinusoidal sweep over the 0–2000 Hz frequency range (see appendix B). The first resonance peak was identified at $f_{\text{tube}} \approx 424\,\text{Hz}$. Although this frequency is relatively low, it remains sufficiently high to capture the energy-containing range and a substantial portion of the inertial subrange. This result suggests that the probe can resolve most of the turbulent kinetic energy before resonance-induced contamination becomes significant, even in the limiting case where no correction is applied; in practice, the probe's built-in correction is applied by default, further mitigating resonance effects.

The smallest scale in the most turbulent flow, estimated by $\eta = \overline{u}/\left(2\pi f_K\right)$, was approximately 0.16 mm (for case C). However, measurements with the Cobra probe are subject to limitations imposed by its spatial resolution. A fundamental limitation stems from the physical spacing of the probe's pressure taps, which is about 1.22 mm (acknowledging the 45° orientation between the probe's head faces). A resolvable frequency (f_{tap}) based on twice this distance would be approximately 380 Hz, suggesting that the probe cannot accurately capture the smallest-scale turbulent eddies. An even more conservative analysis would consider twice the probe's head width as the limiting length scale. In this case, the maximum resolvable frequency (f_{head}) is on the order of 175 Hz. These two spatial limitations (as well as f_{tube}) are graphically represented in figure 6(b), where the Cobra spectra were compared to the HW spectra, which, due to its high spatial resolution but low frequency resolution, experienced only aliasing. Ultimately, the observed deviation in the energy spectra appeared to be primarily associated with the width of the probe head, particularly under high-turbulence conditions. In contrast, the REF case seemed to be more strongly influenced by the spacing of the pressure taps. The probe's physical dimensions were therefore considered to introduce a flow disturbance that altered the local aerodynamic pressure field, thereby corrupting the measurements and explaining the discrepancy between the probes. To support this argument, experiments were conducted at the same location and with the same grids, but at different velocities ($x/D_h = 3.31$ and $Re_{D_h} = [1.59; 1.86; 2.36; 2.58; 2.9] \times 10^4$), to assess the influence of velocity on the frequency associated with the probe head width. The results are shown in figure 7, where the circles correspond to $f_{\text{head}} = \overline{u}/\left(4\pi l_{\text{head}}\right)$. From now on, the spectra shown are smoothed over logarithmically spaced frequency intervals, with the bin density determined by $N = 30\left[\max(u') - \min(u')\right]\left(\overline{u'^2}\right)^{1/2}$. The divergence between the Cobra spectrum and that of the HW appeared to emerge at this frequency, showing, on the one hand, its dependence on the mean flow velocity and, on the other hand, the impact of the probe's physical dimensions.

A fluid-dynamics analysis using the unsteady Bernoulli equation can also help get an idea of the spatial scales at which the steady-state flow assumed in calibration is no longer representative. Based on dimensional analysis, where the characteristic velocity variation is taken as $\partial u(t) \sim \left(\overline{u'^2}\right)^{1/2}$ and the characteristic time scale as $\partial t \sim \eta/\left(\overline{u'^2}\right)^{1/2}$, the temporal contribution in the unsteady Bernoulli equation,

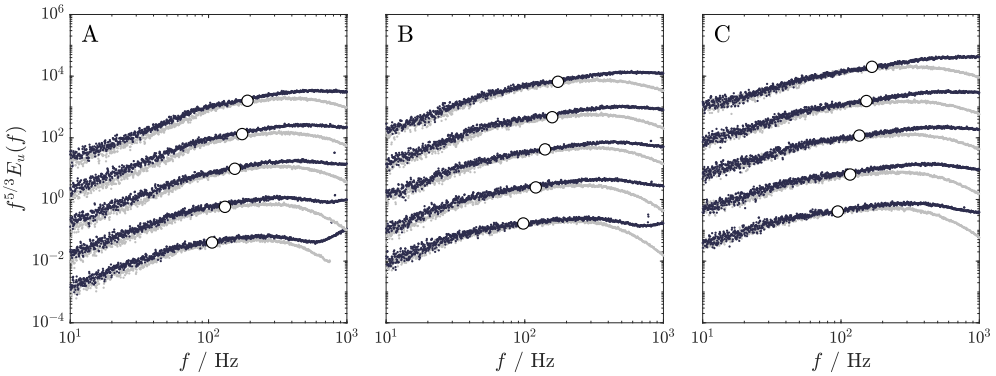

Fig. 7: Semi-compensated energy spectra in frequency space for cases A, B, and C (from left to right). The mean flow velocity increases from bottom to top, and the spectra were shifted by one order of magnitude to improve clarity. The white circles indicate the frequency associated with probe head width, computed using the mean flow velocity.

associated with the pressure variation induced by local fluid acceleration, can be estimated as $\partial u(t)/\partial t \sim \overline{u'^2}/\eta$. This unsteady term becomes significant when the probe's characteristic dimensions are large compared to the smallest flow scales. An order of magnitude analysis shows that the ratio of the unsteady term to the dynamic pressure term:

$$\frac{\rho \int_0^{l_{\text{head}}} \frac{\partial u(t)}{\partial t} dl}{\frac{1}{2}\rho \left(\overline{u}\right)^2} \sim \frac{\overline{u'^2}}{\left(\overline{u}\right)^2} \frac{l_{\text{head}}}{\eta}, \tag{5}$$

yields a value of ~ 0.23 for case C. Although this ratio may appear acceptable, the unsteady term remains of the same order of magnitude as the steady term, indicating that unsteady contributions cannot be neglected. This finding further supports the notion that spatial effects play a significant role in the observed discrepancies.

The approach used to quantify the impact of frequency and spatial limitations was to evaluate their relative contribution to the spectral divergence. The total contribution of aliasing:

$$\Delta_{\text{aliasing}} = \frac{\int_{\text{ISR}} |E_u^a(f) - E_u^{\text{ws}}(f)| \, \mathrm{d}f}{\int_{\text{ISR}} |E_u^c(f) - E_u^{\text{ws}}(f)| \, \mathrm{d}f}, \tag{6}$$

accounted for differences in the inertial subrange (ISR) of approximately 28 %, 9 %, 8 %, and 6 % for REF, A, B, and C, respectively. The contribution of spatial limitations corresponding to $\Delta_{\text{spatial}} = 1 - \Delta_{\text{aliasing}}$, where the contribution from tubing effects was neglected. Although aliasing significantly contributed to divergence at low FST, its influence rapidly decreased across the grid cases as FST increased, thereby indicating that the primary factor driving spectral divergence was the probe geometry itself, including frequency and spatial limitations.

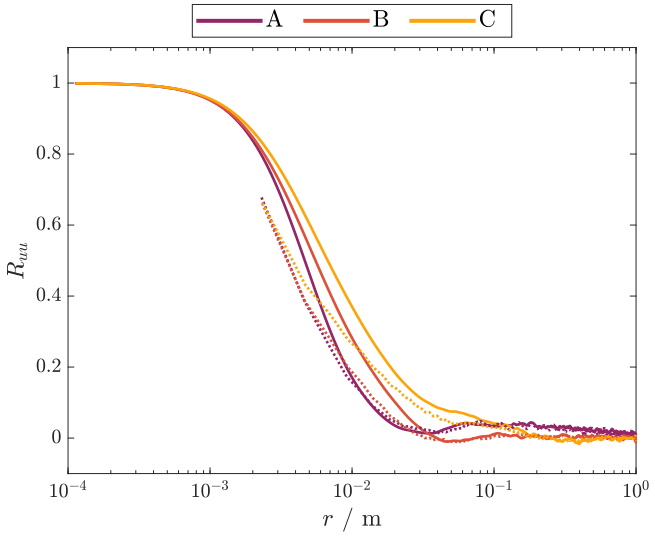

Fig. 8: Autocorrelation functions obtained from HW (plain curves) and Cobra probe (dotted curves) timeseries.

4 Methods

4.1 Integral length scale

Having a sufficiently long temporal signal is generally adequate to capture and achieve convergence of the large-scale features of the flow, even in the case of undersampling. In the context of single-point statistics, one of the most common methods to estimate the integral length scale involves using the temporal autocorrelation function $R_{uu}(\tau) = \overline{u'(t)u'(t+\tau)}/\overline{u'(t)^2}$, which is transformed into a spatial autocorrelation function $R_{uu}(r) = \langle u'(x)u'(x+r)\rangle / \langle u'(x)^2\rangle$ by means of Taylor's frozen turbulence approximation (Taylor, 1938). From this assumption, a characteristic length scale $r = \tau\overline{u}$ can be derived, where τ is the time separation. The streamwise integral length scale is then calculated as $L = \int_0^{r_0} R_{uu}(r)dr$, where $R_{uu}(r_0) = 0$. In some cases, however, the autocorrelation function does not cross zero. The alternative approach involves fitting and integrating an exponential function $\widetilde{R}_{uu}(r) = ae^{-br}$ (Hinze, 1975).

The integral scales measured using the HW were 6.72 mm, 7.73 mm, and 9.68 mm for cases A, B, and C, respectively. For the Cobra probe, L was, respectively, equal to 3.88 mm, 5.37 mm, and 6.10 mm. These correspond to differences of 43 %, 31 % and 37 % for grid A, B, and C respectively. It is important to note that these correlations were based on the fluctuations overestimated by the Cobra probe because of the spectral divergence factors presented in section 3. Consequently, the integral length scale was always underestimated, as $L = \lim\left[\frac{E_u(f)\overline{u}}{4\overline{u'^2}}\right]$ in grid-generated turbulence (Roach, 1987). The difference between the two measurement systems can be visualized in figure 8, where the autocorrelation function derived from the Cobra probe was systematically lower than the one obtained from HW.

4.2 Dissipation scales

Estimating the dissipation scales is essential for characterizing turbulent flows. Under the HIT hypotheses, the turbulent kinetic energy dissipation rate, ε, the Taylor microscale, λ, and the Kolmogorov scale, η, can be computed using the following expressions (Roach, 1987; Frisch, 1995):

$$\varepsilon = 15\nu \left\langle \left(\frac{\mathrm{d}u}{\mathrm{d}x} \right)^2 \right\rangle, \tag{7}$$

$$\lambda = \sqrt{\frac{\overline{u'^2}}{\left\langle \left(\frac{\mathrm{d}u}{\mathrm{d}x} \right)^2 \right\rangle}}, \tag{8}$$

$$\eta = \frac{\nu^{3/4}}{\left[15\nu \left\langle \left(\frac{\mathrm{d}u}{\mathrm{d}x} \right)^2 \right\rangle \right]^{1/4}}. \tag{9}$$

Because the expressions rely on the velocity gradient, high-frequency resolution is required for accurate computation (Roach, 1987). This makes HW anemometry an appropriate tool, whereas the Cobra probe struggles due to its limited resolution. This study aimed to demonstrate that, through appropriate post-processing approaches, the Cobra probe can obtain estimates for the dissipation scales when the onset of the inertial range is known.

4.2.1 Velocity gradient

Assuming small-scale isotropy and Taylor's hypothesis of frozen turbulence, the dissipation rate ε can be estimated using equation 7, where the derivative $\mathrm{d}u/\mathrm{d}x$ can be computed using a finite-difference scheme. However, the accuracy of the differentiation is dependent on the acquisition and physical parameters of the measuring instrument. Wyngaard (1969) showed that the characteristic size of the measuring instrument must be at least on the order of the Kolmogorov scale for accurate estimation. For a two-point statistics setup, as the separation distance between the two acquisition points increases, the accuracy of the measurement deteriorates, as shown by Hussein and George (1990). These findings regarding the influence of spatial separation between two sensors can be extended to the temporal domain through Taylor's frozen turbulence hypothesis. The HW temporal resolution must therefore be sufficiently high to accurately capture the Kolmogorov frequency; however, it also has to be filtered to remove the measurement noise if the sampling frequency is too high. This process, described in section 2.3, ensures that only the turbulence scales related to the flow dynamics are retained. A significant challenge arises with the Cobra probe: its low frequency resolution is analogous to using two HW probes with a wire separation (or wire length) much greater than the Kolmogorov scale. This highlights the need for alternative methodologies to estimate turbulence quantities when the probe's sampling frequency is not sufficient relative to the bandwidth of the measured signal. The consequences of using the velocity gradient for the estimation of dissipation scales are detailed in appendix C.

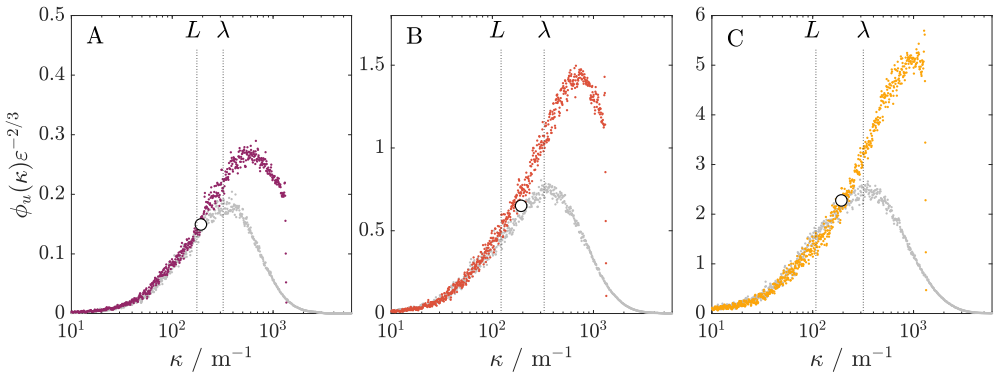

Fig. 9: Compensated spectra for each turbulent case normalized with viscous units. The colored curves are for the unfiltered Cobra probe results, while the light gray curves are for the hot-wire results. The dotted lines represent the inertial subrange with η/L and η/λ forming the boundaries. The white circles indicate the frequency associated with probe head width, computed using the mean flow velocity. Note that the y-axis scale differs between panels.

4.2.2 Kolmogorov's 1941 phenomenology

The formalism introduced by Kolmogorov (1941), combined with Taylor's frozen turbulence hypothesis, enables the redefinition of the one-dimensional spectra shown in figure 4 in wavenumber space as:

$$E_u(\kappa) = C_\kappa \varepsilon^{2/3} \kappa^{-5/3}, \tag{10}$$

where C_κ is the 1D Kolmogorov constant. Sreenivasan (1995) showed the quasi-universality of this constant by gathering the results of multiple studies. The author showed that this constant is approximately equal to 0.53 for $Re_\lambda > 50$. For lower Re_λ, the experimental results suggested that C_κ follows an increasing trend. This last statement is relevant to the present study as the experimental conditions correspond to relatively low Re_λ. A practical method to determine the dissipation rate consists of fitting equation 10 to the wavenumber-space spectra. This approach is based on the property of the constancy of the dissipation rate in the inertial subrange. However, as ε is unknown for now, only a 1D semi-compensated spectrum could be defined by normalizing the spectrum with the wavenumber:

$$\phi_u(\kappa)\varepsilon^{2/3} = E_u(\kappa)\kappa^{5/3}. \tag{11}$$

The left-hand side can thus be evaluated from the inertial range characterized by the region where the compensated spectrum remains reasonably constant. The semi-compensated spectra of the three turbulent cases are presented in figure 9. For the HW data, one might assume that the $C_\kappa \varepsilon^{-2/3}$ corresponds to the peak value of the $\phi_u(\kappa)\varepsilon^{-2/3}$ curve. However, it is important to note that in all three cases, the inertial range seemed to have shifted leftward compared to the peak (which occurred close

to the Taylor scale). Consequently, the expected plateau in the inertial range did not appear, and the peak could not be associated with C_κ (Donzis and Sreenivasan, 2010). This is not something new and can be explained through several interconnected reasons. Despite a slight increase in size with FST (see figure 9), the overall extent of the inertial subrange remained very limited due to the small dimensions of the wind tunnel. The spectra did not show the theoretical plateau predicted by Kolmogorov (1941), suggesting a weak scalability at low Re_λ (Mydlarski and Warhaft, 1996; Bodenschatz et al., 2014). Then, the spectral peak is linked to a phenomenon called the *bottleneck effect*. This effect was extensively studied in the literature (Saddoughi and Veeravalli, 1994; Sreenivasan, 1995; Lohse and Müller-Groeling, 1995; Verma and Donzis, 2007; Donzis and Sreenivasan, 2010; Su et al., 2023). Sreenivasan (1995) explained that this effect takes place when the constant energy flux across the inertial range is combined with rapid viscous damping, leading to an energy accumulation at the transition between the inertial and the dissipation ranges. Verma and Donzis (2007) reported that there needs to be a wide range of scales for the energy to be transferred properly from large to small scales. Their work showed that the inertial range must span at least four decades of frequency for this effect to become negligible, which was clearly not the case in this study. The authors suggested that this bump could be seen as a compensation for the absence of the required inertial subrange and for the progressive decrease in energy transfer efficiency at these scales due to the beginning of viscosity damping (temporary slowdown of the energy cascade due to energy transfer inefficiency). Isaza et al. (2014) showed that decreasing Re_λ led to a reduction of the plateau and a progressive steepening of the inertial range. Additionally, Bodenschatz et al. (2014) observed a gradual extension and flattening of the inertial subrange as Re_λ increased. Given the unknown extent of the bottleneck effect in the present study and the low Re_λ, the proposed approach to mitigate its influence was to fit equation 10 within the inertial region (ranging from L to λ) of the experimental data using the dissipation rate previously calculated. This was regarded as a sufficiently accurate and simple preliminary estimation, aligning with Mydlarski and Warhaft (1996), who reported that C_κ falls approximately within the lower and upper bounds of the scaling range.

The Kolmogorov constant would therefore be computed by fitting the Kolmogorov model to the experimental data using a nonlinear least-squares method with an initial condition of $C_\kappa = 0.53$. However, as it can be deduced from figure 9, this fitting would yield a different constant for the HW and Cobra spectra because of the spectral divergence. To obtain values more aligned with expected results, it was necessary to adjust the Cobra probe spectra by compensating for the excessive nonphysical energy contributions. The approach to achieving this goal involved determining whether a general correction function could be identified for the three turbulence cases. Then, another critical issue is that determining C_κ is only possible if ε is known, which was not the case here for the reasons outlined earlier in section 4.2.1. The following sections are therefore intended not only to identify a way to correct the spectrum but also to estimate the dissipation rate using empirical methods instead of the classical way using the velocity gradients.

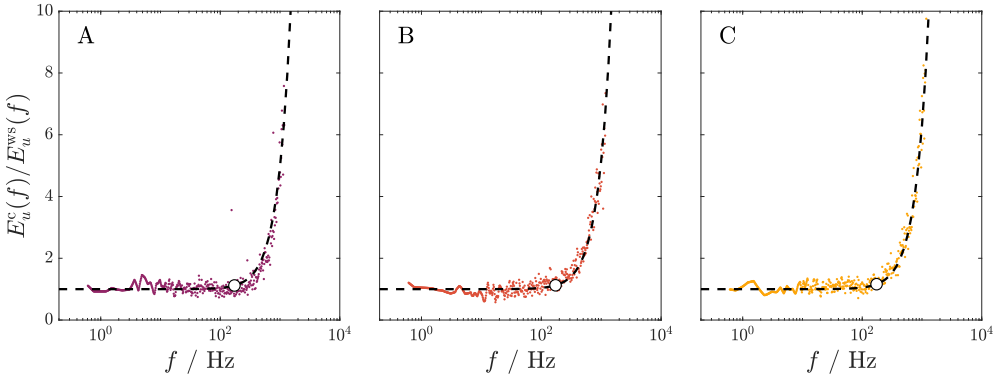

Fig. 10: Relative comparisons between Cobra undersampled energy spectra, $E_u^c(f)$, and HW well-sampled energy spectra, $E_u^{ws}(f)$, for all turbulence cases. The dark dashed line depicts a second-order polynomial correction function $H(f) = 1 + af^2$, where a was obtained by fitting $H(f)$ to the present spectral ratios. For the flow conditions of the current study, $a = 3.97 \times 10^{-6}$ for case A, $a = 4.16 \times 10^{-6}$ for case B, and $a = 5.30 \times 10^{-6}$ for case C. The white circles indicate the frequency associated with probe head width, computed using the mean flow velocity.

5 Results and discussion

5.1 Correction function

The ratios between the undersampled Cobra spectra ($E_u^c(f)$) and the well-resolved HW spectra ($E_u^{ws}(f)$) are presented in figure 10. For grids A, B, and C, the ratio displays a comparable behavior, increasing quadratically from the frequency associated with the probe head size. On this basis, the ratio between the two energy spectra could be represented by a quadratic correction function depending solely on a single parameter a:

$$H(f) = 1 + af^2. \tag{12}$$

For the three cases considered in the present study, the coefficient a took relatively similar values ($a = 3.97 \times 10^{-6}$ for case A, $a = 4.16 \times 10^{-6}$ for case B, and $a = 5.30 \times 10^{-6}$ for case C). One might be inclined to regard this coefficient as identical across all cases; however, as demonstrated in section 3, the deviation of the Cobra spectrum from that of the HW occurs at the frequency associated with the probe size, which itself depends on the mean flow velocity. Intuitively, this suggests that the coefficient is more likely to vary with the mean flow velocity. To verify this assumption, the initial three cases, the measurements previously used to construct figure 7 and additional measurements along the test section ($Re_{D_h} = 1.8 \times 10^4$, $x/D_h = [0.74, 1.47, 2.21, 2.94, 3.68, 4.41, 5.15]$) were analyzed. By fitting a least-squares law in the logarithmic domain to these data, it was possible to derive an empirical relationship between the coefficient a and the mean flow velocity, expressed as follows:

$$\log_{10}(a) = A \log_{10}(\overline{u})^{-B}, \quad A = -5.602, \quad B = -0.1937. \tag{13}$$

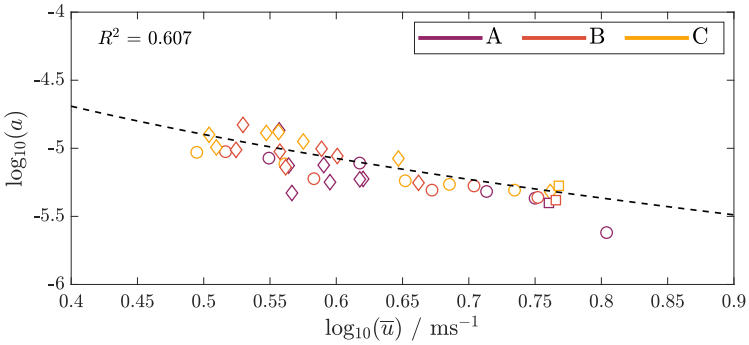

Fig. 11: Coefficient a obtained by fitting equation 12 to the ratio of the Cobra spectrum to the HW spectrum as a function of the measured mean flow velocity. □: $x/D_h = 3.31$ and $Re_{D_h} = 2.6 \times 10^4$; ○: $x/D_h = 3.31$ and $Re_{D_h} = [1.59; 1.86; 2.36; 2.58; 2.9] \times 10^4$; ◊: $Re_{D_h} = 1.8 \times 10^4$ and $x/D_h = [3.68, 4.41, 5.15]$; ---: Equation 13. The quality of the fit between experimental data and the empirical model is expressed by the coefficient of determination, R^2.

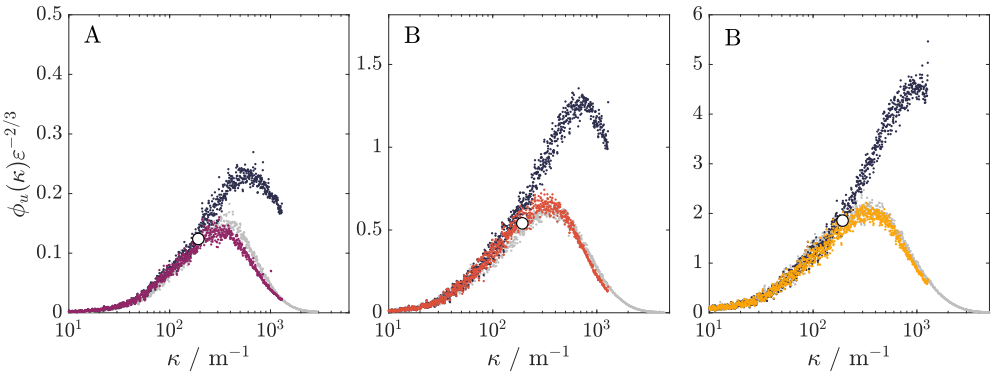

Fig. 12: Semi-compensated spectra for each turbulent case. The colored curves are the corrected Cobra probe spectra, the light gray curves are the hot-wire spectra, and the dark gray curves are the raw Cobra spectra. The white circles indicate the frequency associated with probe head width, computed using the mean flow velocity.

Starting from equation 12, it is then possible to redefine the correction function as a function of the mean flow velocity, such that:

$$H(f, \overline{u}) = 1 + 10^{\left(-5.602 \log_{10}(\overline{u})^{0.1937}\right)} f^2 \tag{14}$$

The compensated spectra obtained after applying the correction are presented in Figure 12. Apart from a minor deviation in case A, the inertial range shows a substantially improved agreement. In section 4.1, the integral length scale was shown to be underestimated because of the spectral divergence. By applying the correction, the

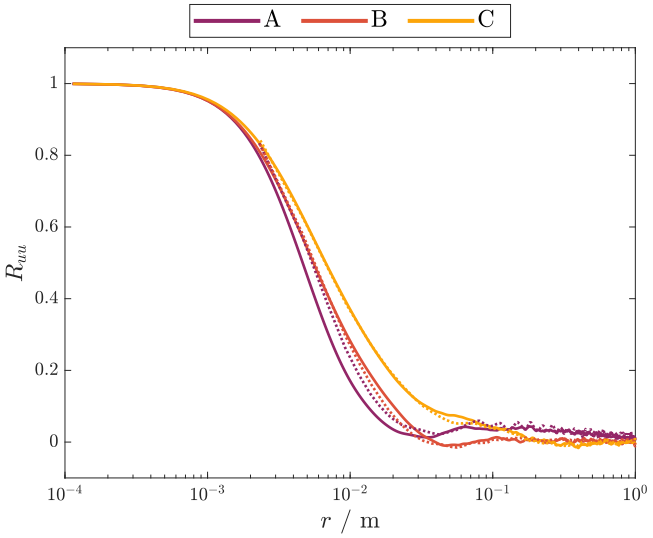

Fig. 13: Autocorrelation functions obtained from HW (plain curves) and corrected Cobra probe results (dotted curves).

Table 3: Comparison of the RMS fluctuations and integral length scale for the HW signals, and the Cobra probe signals before and after the correction using equation 14.

		Hot-Wire			Cobra Probe (CP)			CP corrected		
		A	B	C	A	B	C	A	B	C
$\sqrt{\overline{u'^2}}$	(ms^{-1})	0.107	0.243	0.486	0.122	0.277	0.518	0.107	0.241	0.455
L	(mm)	6.72	7.73	9.68	3.88	5.37	6.10	7.76	8.14	10.07

excessive contribution from the pressure probe limitations could be reduced. Using equation 3, it was therefore possible to reassess the RMS of the velocity fluctuations. These new signals could also be used to reevaluate the autocorrelation function (after applying an inverse fast Fourier transform on the corrected frequency-domain signal), enabling a more accurate estimation of the integral length scale. The new autocorrelation functions are presented in figure 13. Unlike figure 8, the corrected autocorrelation functions aligned much better with those obtained from the HW, allowing for improved estimations for L. The new values for the RMS fluctuations and the integral length scales are presented in table 3. These exhibited good consistency between the HW and the corrected Cobra probe results. The streamwise RMS fluctuations obtained from corrected Cobra signals slightly differed from the HW measurements by 0.1%, 0.7%, and 6.4% (against 14.3%, 13.9%, and 6.6% for the raw Cobra timeseries) for A, B, and C, respectively. The integral length scale was also better estimated, as shown by the new deviations from the HW values of 15.5%, 5.3%, and 4.03% for cases A, B, and C, respectively. These deviations were markedly smaller than those reported in section 4.1, thus reflecting the improvement brought by the correction.

5.2 Dissipation constant

After applying the correction, a more reliable estimate for the integral length scale could be obtained (table 3). The aim was thus to establish an empirical relation connecting this value to the turbulence dissipation scales. To this end, the dissipation scaling of the equilibrium energy cascade introduced by Taylor (1935) and Kolmogorov (1941) was employed. Within this framework, the dissipation constant, C_ε, which links the dissipation time scale to the characteristic time scale of the large eddies, can be defined as

$$\varepsilon = C_\varepsilon \left(\overline{u'^2}\right)^{3/2} L^{-1}. \tag{15}$$

Crucially, C_ε is not universal but depends on the turbulence regime: values around 0.5 have been reported for shear turbulence (Pearson et al., 2002; Obligado et al., 2022; Nedić et al., 2017), whereas grid turbulence generally yields values close to 1.0 (Sreenivasan, 1984, 1995). The expression for ε can be rewritten so that $\varepsilon = 15\nu\overline{u'^2}/\lambda^2$. By using Re_λ, the expression for the dissipation constant then becomes:

$$C_\varepsilon = \frac{L}{\lambda}\frac{15}{Re_\lambda}, \tag{16}$$

where the equilibrium scaling, $L/\lambda \propto Re_\lambda$, is only valid in the far field of HIT flows (Isaza et al., 2014; Zheng et al., 2023). The ratios L/λ for the initial three cases, as well as for the cases shown in figure 7 and for the streamwise results, are presented in figure 14. Two empirical relationships were plotted on this figure. The first, proposed by Isaza et al. (2014), describes the evolution of L/λ using a first-order polynomial, $L/\lambda = 0.0368Re_\lambda + 1.8$, under HIT hypotheses and assuming that the far field begins at $x/M \sim 12$ (Isaza et al., 2014). The second relationship is directly derived from a modified version of the theoretical prediction by Lohse (1994) for estimating the dissipation constant:

$$C_\varepsilon = C_{\varepsilon,\infty}\sqrt{1 + \frac{5}{4}\frac{\gamma^3}{Re_\lambda^2}}, \tag{17}$$

where $\gamma = 14$ and $C_{\varepsilon,\infty} = (9/\gamma)^{3/2}$. Except for some low-Reynolds-number outliers, the values obtained with the HW follow the modified prediction of Lohse (1994) more closely than the linear relationship proposed by Isaza et al. (2014). One value tended to deviate from the curve as Re_λ increased; this corresponds to a case for which x/M was relatively small, indicating proximity to the near-field. For points that were too close to the passive grid, the classical dissipation laws would not hold, and thus the empirical relationships presented here would need to be adjusted to take into account non-equilibrium dissipation scaling (Isaza et al., 2014; Zheng et al., 2023). These results were presented in figure 15 and compared with data from other studies (Sreenivasan, 1984; Obligado et al., 2022; Nedić et al., 2017). The main conclusion was that the measurements closely followed the empirical prediction and fell well within the cluster of literature values. However, these results were obtained from the HW, which was sufficiently resolved to provide reliable estimates using velocity gradients. The next objective was to derive these quantities from the Cobra probe measurements, for which velocity gradients cannot be used due to the low acquisition frequency and the strong

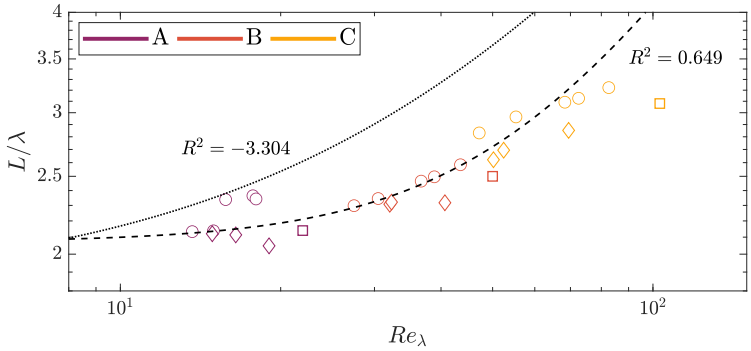

Fig. 14: Integral and Taylor length scales ratio versus Reynolds number based on Taylor microscale. These results were obtained from the hot-wire measurements. □: $x/D_h = 3.31$ and $Re_{D_h} = 2.6 \times 10^4$; ○: $x/D_h = 3.31$ and $Re_{D_h} = [1.59; 1.86; 2.36; 2.58; 2.9] \times 10^4$; ◊: $Re_{D_h} = 1.8 \times 10^4$ and $x/D_h = [3.68, 4.41, 5.15]$. $\cdots$: Isaza et al. (2014); - - -: Modified Lohse (1994). The quality of the fit between experimental data and the two empirical models is expressed by the coefficient of determination, R^2 ($R^2 = 1$ indicates a perfect fit).

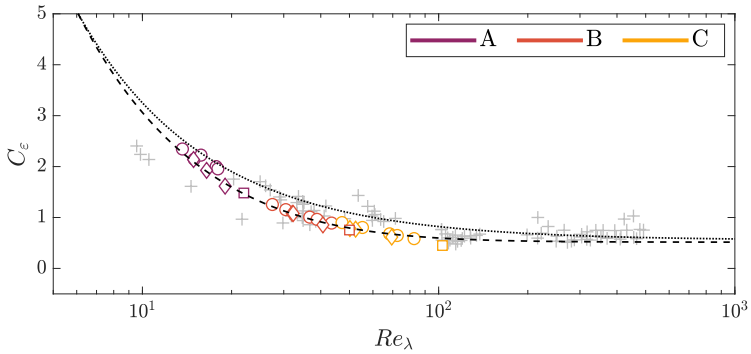

Fig. 15: Dissipation constant versus Reynolds number based on Taylor microscale. These results were obtained from the hot-wire measurements. □: $x/D_h = 3.31$ and $Re_{D_h} = 2.6 \times 10^4$; ○: $x/D_h = 3.31$ and $Re_{D_h} = [1.59; 1.86; 2.36; 2.58; 2.9] \times 10^4$; ◊: $Re_{D_h} = 1.8 \times 10^4$ and $x/D_h = [3.68, 4.41, 5.15]$. $\cdots$: Isaza et al. (2014); - - -: Modified Lohse (1994). +: Compilation of passive grids flow studies gathered in Sreenivasan (1984) and dissipation coefficients in turbulent boundary layer from Obligado et al. (2022) and Nedić et al. (2017).

dependence of the gradient-based estimate on the cutoff frequency (see section C5). To address this, by substituting equation 17 into equation 15 and using equations 7

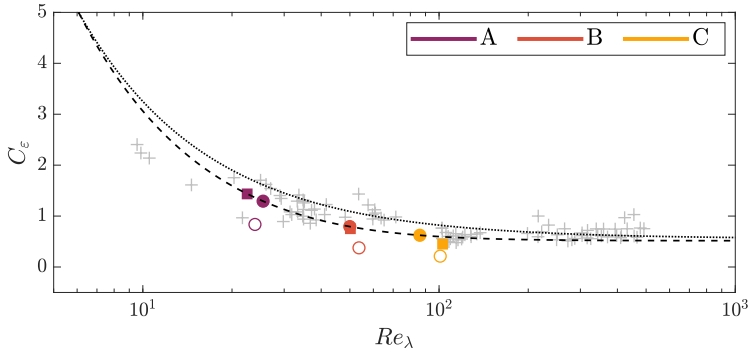

Fig. 16: Dissipation constant versus Reynolds number based on Taylor microscale. ○: Present raw Cobra results computed using the velocity gradient ($n = 3$); ●: Present corrected Cobra results; ■: Present hot-wire results. · · · : Isaza et al. (2014); - - -: Modified Lohse (1994). +: Compilation of passive grids flow studies gathered in Sreenivasan (1984) and dissipation coefficients in turbulent boundary layer from Obligado et al. (2022) and Nedić et al. (2017).

and 8, it was possible to obtain an expression such that:

$$\frac{15\nu L}{\lambda^2 \left(\overline{u'^2}\right)^{1/2}} = C_{\varepsilon,\infty}\sqrt{1+\frac{5}{4}\frac{\gamma^3}{Re_\lambda^2}} \tag{18}$$

Here, the only unknown is λ. Once λ was assessed by solving the equation, it was then possible to estimate the dissipation rate ε and the Kolmogorov length scale using equations 7 and 9, respectively. The results of this procedure applied to the Cobra probe data are shown in figure 16. Values obtained using the velocity gradient with a sixth-order accuracy scheme ($n = 3$) were compared to those obtained after correction using the empirical methodology. The comparison revealed that the Cobra measurements based on the velocity gradient tended to underestimate the expected values, due to inaccurate estimates of L and $\left(\overline{u'^2}\right)^{1/2}$. After applying the correction, however, the estimation of C_ε improved. The estimates of C_κ could, however, be computed using the methodology explained in section 4.2.2. Similarly, the values obtained with the velocity gradient, and the values obtained after correcting the Cobra probe signal were compared to the HW results and to data compiled from various sources in Sreenivasan (1995). These are shown in figure 17. The HW results aligned relatively well with the cluster of points reported in the literature, except for the point corresponding to the highest turbulence level, which appeared to be a bit out of the trend for the same reason as in the previous paragraph. Regarding the values derived from the raw Cobra signals using the velocity gradient, there seemed to be a general tendency for these values to be overestimated this time. However, once the correction was applied, the spectrum would more effectively replicate the bottleneck effect observed with the HW. The corrected results clearly indicate that the estimates obtained after the use of

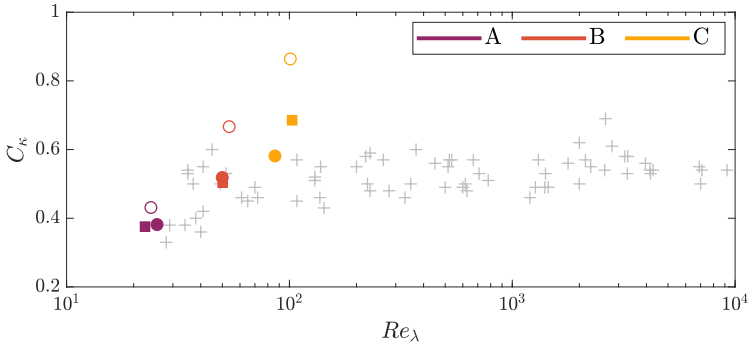

Fig. 17: Kolmogorov constant versus Reynolds number based on Taylor microscale. ○: Present raw Cobra results computed using the velocity gradient ($n = 3$); ●: Present corrected Cobra results; ■: Present hot-wire results; +: Compilation of studies on various types of flow gathered in Sreenivasan (1995).

the proposed corrections would therefore converge toward those predicted by the HW measurements. It should be noted that values derived from raw Cobra probe measurements using the velocity gradient may, in certain cases, appear reasonable. However, these values were obtained at a relatively high cutoff frequency. Since the cutoff frequency directly influences the gradient, the discrepancy reported in this study can be regarded as the minimum difference achievable with this approach. Consequently, the results presented here should be considered conservative when compared to the potentially larger discrepancies that may arise from relying on velocity gradients.

A summary of the turbulence statistics is presented in Table 4. Overall, the estimated turbulence quantities showed good agreement between the HW and the corrected Cobra probe results. As observed in figure 17, case C exhibited the largest deviations from the HW values, highlighting a limitation of the method for cases that act as outliers, i.e., those further from the predictions of equation 17. This discrepancy is likely linked to the measurement location. Indeed, in figure 14, the yellow square representing case C (at $Re_\lambda = 103$) fell slightly off the curve because the grid wake was not fully developed yet at that position ($x/M \sim 9$ against $x/M \sim 12$ for the beginning of the far-field according to Isaza et al. (2014)). Consequently, case C remained in the transitional region between near- and far-field, leading to deviations from equilibrium dissipation laws. This explained the less accurate estimates for the turbulence scales and demonstrated that the method applies primarily to fully developed, far-field turbulence.

6 Applicability in a larger wind tunnel

This study presented methods to facilitate the estimation of turbulence quantities using a Cobra probe, despite the typical limitations imposed by its low sampling frequency and the size of the probe head. Although these methods required prior calibration with an HW to correct the inertial subrange, they provided reasonable first estimates of key turbulence parameters. However, until now these methods have

Table 4: Final turbulence statistics derived from HW and Cobra probe corrected signals.

		Hot-Wire			CP corrected		
		A	B	C	A	B	C
λ	(mm)	3.12	3.07	3.14	3.53	3.08	2.81
Re_λ	(−)	22	50	103	25	50	86
η	(mm)	0.33	0.22	0.16	0.36	0.22	0.15
ε	(m^2s^{-3})	0.26	1.40	5.33	0.21	1.37	5.82
C_ε	(−)	1.44	0.75	0.45	1.29	0.79	0.62
C_κ	(−)	0.37	0.50	0.69	0.38	0.52	0.58

been applied primarily to a single type of flow in a small-scale wind tunnel (SSWT) with a cross-section of 0.068 m × 0.068 m. The drawback of using such a small tunnel under standard atmospheric conditions is that the cross-section itself limits the width of the inertial subrange, since the large eddies cannot physically exceed a size related to the tunnel width. So far, these methods have proven effective in the context of this small facility. The next step is therefore to investigate whether they can also perform reliably when applied in a larger-scale wind tunnel.

To this end, additional experiments were conducted in the large-scale multidisciplinary wind tunnel of the University of Liège. This closed-loop facility features two test sections, TS1 and TS2, the latter being larger in size, with the two sections separated by a cross-section expansion. The detailed dimensions of the wind tunnel are reported in Vita et al. (2018). HW and Cobra measurements were carried out under the same acquisition parameters as described in section 2. Both probes were operated simultaneously along the tunnel centerline at positions $x_{\mathrm{TS1}} = [1.5; 3; 4]$ m in TS1 and $x_{\mathrm{TS2}} = [11; 12; 13; 14; 15; 16]$ m in TS2, for three freestream velocities $U_\infty \sim [3; 5; 8]$ m/s. Three turbulence grids were employed to generate turbulent flow conditions. In order of increasing turbulence intensity, these correspond to grid Aa, Bb, and Cc (noted as #3, #2, and #4, respectively, in Vita et al. (2018)). Their characteristics, as well as the turbulence conditions they generate, are described in Vita et al. (2018). To ensure that measurements were at least in the onset of the far-field, data with $x/M < 10$ were excluded. The objective of combining measurements acquired at different positions, velocities, and behind different grids was not to perform a complete new characterization, but rather to demonstrate that the proposed methodology applied to another set of turbulent flow conditions.

First, the question of the probe's limitations must still be addressed. To verify whether the correction law expressed in equation 14 remained valid, the spectra obtained from the Cobra probe were divided by those obtained from the hot-wire for all flow configurations in the large-scale wind tunnel (LSWT). The results are again presented in terms of the coefficient a as a function of the mean flow velocity in figure 18. The coefficients measured in the LSWT generally followed the trend already identified in figure 11, except for a certain scattering at lower velocities. The coefficient was expected to follow the previously defined law, since the primary parameter influencing the deviation of the Cobra spectrum from the HW spectrum depends on a frequency

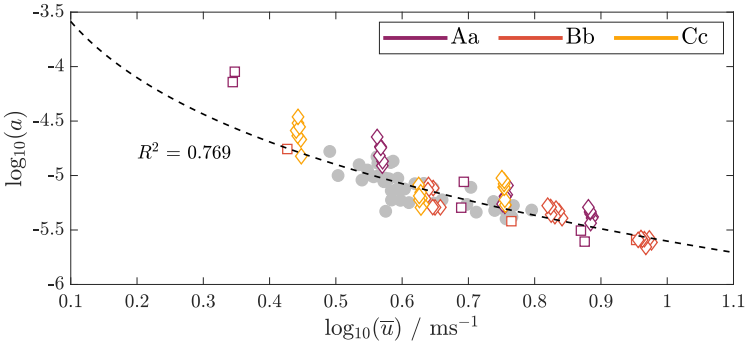

Fig. 18: Coefficient a obtained by fitting equation 12 to the ratio of the Cobra spectrum to the HW spectrum as a function of the measured mean flow velocity. The colored empty symbols are for the LSWT results. The filled light gray circles are for the SSWT. □: TS1 results; ◊: TS2 results; - - -: Equation 13. The quality of the fit between experimental data (colored symbols) and the empirical model is expressed by the coefficient of determination, R^2 ($R^2 = 1$ indicates a perfect fit).

associated with the probe size and thus on the mean flow velocity. This figure confirmed that the coefficient does not necessarily, or at least only weakly, depend on the characteristic scale of the flow domain in which the measurements are performed.

Similarly, the ratio L/λ (based on values measured with the HW) was plotted against the results obtained in the SSWT in figure 19. The results showed a general tendency to follow the modified theoretical prediction of Lohse (1994), although they also aligned a bit more closely with the empirical law proposed by (Isaza et al., 2014). Figure 20 further indicates that the dissipation constants remained tightly clustered with the values of the literature. The modified theoretical prediction of Lohse (1994) was kept, as it provided a reasonable representation of the LSWT values, particularly at low Re_λ.

Finally, the relative errors between the dissipation rates obtained after correcting the Cobra signals and the expected dissipation rates (derived from velocity gradients with the HW) are shown in figure 21. The relative errors in the small-scale wind tunnel are represented as filled gray circles. Beyond a slight tendency for stronger turbulence to reduce the relative error, the main conclusion is that the dissipation rates—and, indirectly, other statistical quantities under HIT assumptions—could be estimated with a relative error generally below 30% for the tested conditions. Although this error may appear significant, it should be emphasized that these are estimates of turbulence quantities based on statistical methods, where imperfections can strongly influence the outcome. Considering the practical advantages of the Cobra probe, the fact that gradient-based methods are avoided, and the technical constraints associated with HW measurements are eliminated, this level of error is deemed acceptable for the estimation of turbulence quantities.

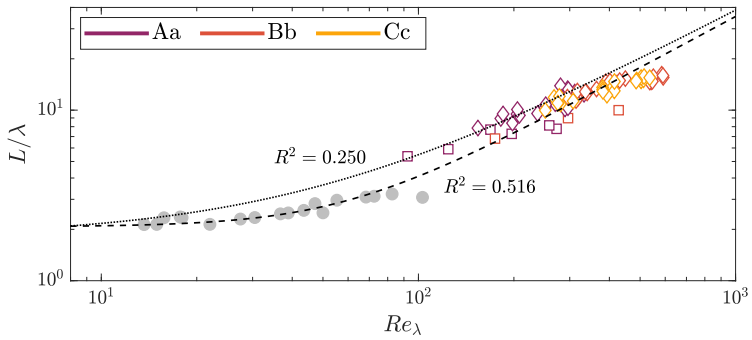

Fig. 19: Integral and Taylor length scales ratio versus Reynolds number based on Taylor microscale. These results were obtained from the hot-wire measurements. The colored empty symbols are for the LSWT results. The filled light gray circles are for the SSWT. □: TS1 results; ◊: TS2 results. · · · : Isaza et al. (2014); - - -: Modified Lohse (1994). The quality of the fit between experimental data (colored symbols) and the two empirical models is expressed by the coefficient of determination, R^2 ($R^2 = 1$ indicates a perfect fit).

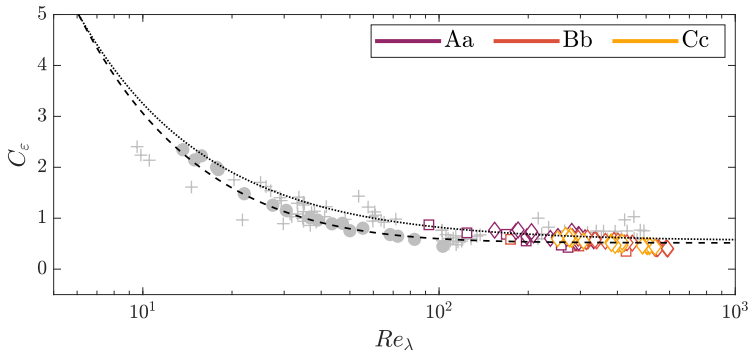

Fig. 20: Dissipation constant versus Reynolds number based on Taylor microscale. These results were obtained from the hot-wire measurements. The colored empty symbols are for the LSWT results. The filled light gray circles are for the SSWT. □: TS1 results; ◊: TS2 results. · · · : Isaza et al. (2014); - - -: Modified Lohse (1994). +: Compilation of passive grids flow studies gathered in Sreenivasan (1984) and dissipation coefficients in turbulent boundary layer from Obligado et al. (2022) and Nedić et al. (2017).

7 Conclusion

Turbulence characterization measurements were conducted in a newly designed, small-scale wind tunnel aimed at studying low-Reynolds-number flows. The timeseries were acquired at a Reynolds number of $Re_{D_h} = 2.6 \times 10^4$ on the centerline at mid-length of the test section. The turbulence level of the clean test section was reported to be

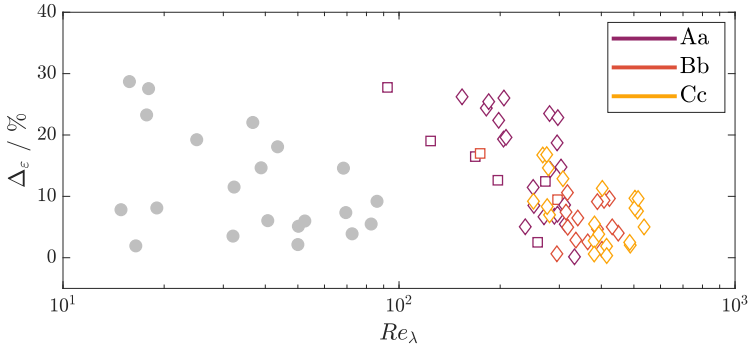

Fig. 21: Relative difference between the estimated dissipation rate obtained with the Cobra probe and the expected dissipation rate from HW measurements. The filled light gray circles correspond to results in the SSWT. □: TS1 results; ◊: TS2 results.

below 0.5 %. Three passive turbulence grids were studied: A ($T_i \approx 2\,\%$), B ($T_i \approx 4\,\%$), and C ($T_i \approx 8\,\%$). Hot-wire anemometry was employed to establish benchmark turbulence statistics for the three cases. These reference values were then compared with turbulence estimates obtained using a Cobra probe, which, despite its lower sampling rate, offers practical advantages: robust, geometry-dependent pre-calibration and simultaneous acquisition of all three velocity components. These features make the Cobra probe a convenient tool for turbulence measurements in this compact wind tunnel setup and in many other experimental aerodynamic configurations.

Two principal limitations of the Cobra probe, and all the pressure probes in general, were identified. The first concerns its restricted sampling frequency, which results in undersampling, aliasing, and frequency folding. The second arises from the probe's physical configuration: the geometrical constraints of the probe likely induce flow disturbances that contaminate high-frequency measurements. Together, these effects generate spectral deviations at frequencies linked to the probe head width, producing artificially elevated fluctuation levels and biasing turbulence statistics such as the integral length scale (L), the Taylor microscale (λ), the Kolmogorov scale (η), and the dissipation rate (ε). Consequently, the Cobra probe is generally unsuitable for direct estimation of turbulence quantities using velocity derivatives. The present study, however, sought to develop post-processing strategies that enable the recovery of these quantities while retaining the practical benefits of the Cobra probe and avoiding the experimental challenges associated with hot-wire anemometry

Since divergence between the Cobra and hot-wire spectra consistently emerged at frequencies associated with the probe head width and the mean flow velocity, an empirical second-order polynomial correction was devised to adjust the Cobra spectrum. This correction improved estimates of the integral length scale (L) and the RMS velocity fluctuations. Furthermore, by combining equilibrium cascade scaling for homogeneous isotropic turbulence with a modified version of the theoretical prediction of the dissipation constant of Lohse (1994), a solvable relationship was obtained that yielded estimates of the Taylor microscale (λ). Under the HIT assumptions, this also permitted the estimation of the Kolmogorov scale (η) and the dissipation rate (ε),

quantities typically accessible only with highly resolved measurements. The method was validated in the large-scale wind tunnel at the University of Liège, showing that dissipation estimates obtained exclusively from corrected Cobra signals can achieve relative errors below 30 % when compared with hot-wire measurements.

Overall, the methods proposed here enabled reliable estimation of key turbulence quantities despite the intrinsic limitations of the Cobra probe. The results demonstrate that the Cobra can serve as a practical alternative to hot-wire anemometry, leveraging the advantages of a pressure probe without relying on conventional velocity gradient measurements. Nevertheless, the empirical corrections employed in this work were calibrated against hot-wire data under specific experimental conditions. Although validation was performed at two different wind tunnel scales, the broader applicability of these methods remains to be confirmed. In particular, it is expected that this procedure could be applied to any type of pressure probe, provided that both the frequency and physical limitations of the probe are taken into account. Indeed, probes of different sizes will likely require probe-specific empirical relations for the correction coefficient a, and the approach may need to be adapted for flows other than grid-generated turbulence, where the dissipation constant $C_{\varepsilon,\infty}$ may not converge to a similar constant value.

Acknowledgments. This work has been supported by the "Actions de Recherche Concertées" *DustInTheWind* funded by "Fédération Wallonie Bruxelles" in Belgium (reference: ARC 23/27-10).

Author contributions. Simon Dehareng contributed to experimental testing, investigation, and writing (original draft). Thomas Gemine contributed to the design/building of the wind tunnel and investigation. Geoffroy Lumay contributed to writing review and supervision. Thomas Andrianne contributed to writing review and supervision. All authors have read and agreed to the published version of the manuscript.

Declarations

Conflict of interest. The authors have no conflict of interest to declare that are relevant to the content of this article.

Appendix A Flow homogeneity

The evolution of turbulence characteristics was evaluated at 7 points distributed along the centerline, $x/D_h = [0.74, 1.47, 2.21, 2.94, 3.68, 4.41, 5.15]$. For each case, the mean velocity in these locations gradually increased due to the boundary layer growth and continuity. The turbulence intensity remained around 0.45 % for the REF case, decayed from 3.2 % to 1.4 % for A, from 7.5 % to 3.5 % for B, and from 15.8 % to 5.8% for C. For the three grid cases, the decays followed the empirical laws based on bar width described in Laneville (1973).

The homogeneity of the flow in the y–z plane was assessed through planar measurements conducted at the mid-length of the test section. These measurements were performed on a $0.4D_h \times 0.4D_h$ grid oriented perpendicular to the flow direction. The

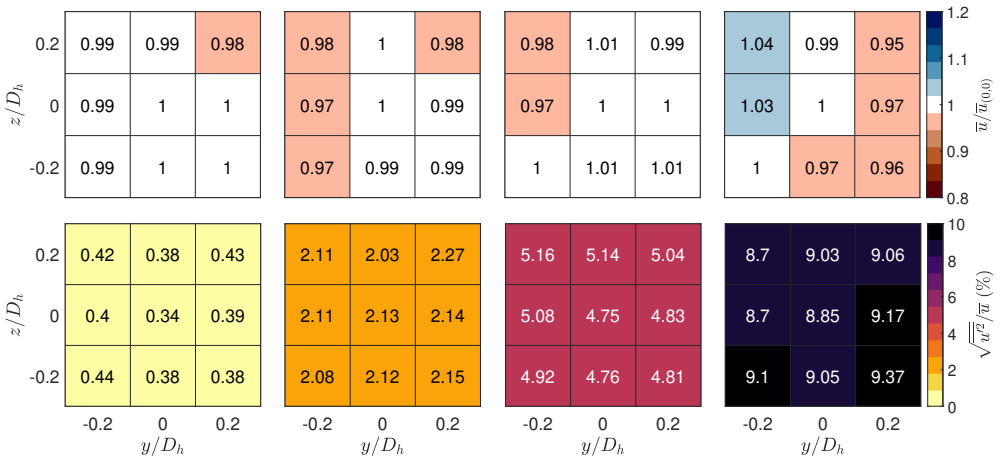

Fig. A1: Homogeneity of the flow in a $0.4D_h \times 0.4D_h$ array at mid-length of the test section for REF, A, B, and C cases from left to right, respectively. The values for $\overline{u}$ (top) are normalized by the respective centerline velocity $\overline{u}_{(0,0)}$. The bottom values represent the turbulence intensities expressed as a percentage.

analysis focused on nine points distributed around a central reference point, which is the location of interest for the study. Figure A1 presents the distribution of the mean and fluctuating velocity components across the measurement grid. Overall, the results indicate that the mean velocity remained homogeneous within ±5% of the centerline velocity, with turbulence intensity exhibiting reasonable uniformity.

Appendix B Probe correction function

Figure B2 compares the experimental Cobra probe correction function to the model of Bergh and Tijdeman (1965), assuming a transducer cavity volume of $V_{\text{tr}} \approx 20$ mm^3 (based on the fit of the model to the results presented in Hooper and Musgrove (1997)), and a tube length of approximately 120 mm. The resonance frequency is defined as the frequency corresponding to the first peak in the magnitude of the transfer function, $|G(i\omega)|$:

$$f_{\text{tube}} = \arg\max_{f} \left|G(i\omega)\right|. \tag{B1}$$

Appendix C Velocity gradient & undersampling

Figure C3 illustrates the evolution of the ensemble-averaged squared velocity gradient, calculated using a two-point forward difference method as a function of the cutoff frequency, f_c. The two curves were derived from unfiltered time series measured with the Cobra and the HW with the turbulence grid B. Looking at the HW curve, the convergence of the velocity gradient was achieved when the signal was filtered at the Kolmogorov advection frequency (visual representation of the iterative filtering process

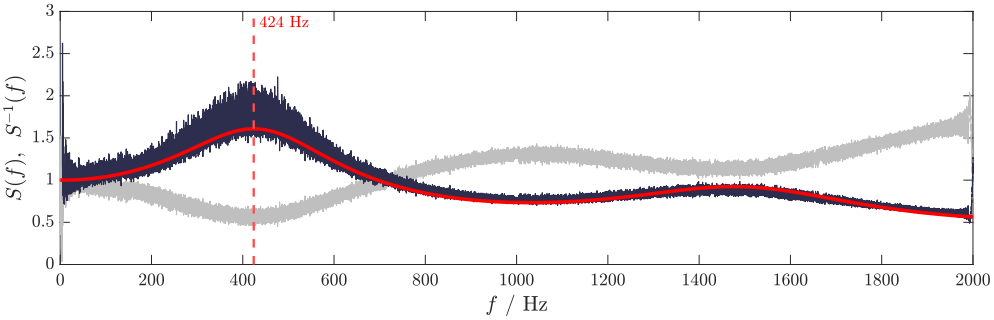

Fig. B2: (Light gray) Frequency response function of the Series 100 Cobra probe to a constant-amplitude sinusoidal sweep, $S(f) = \left|\mathcal{F}\{p_{\mathrm{sig}}(t) - \overline{p}_{\mathrm{sig}}\}(f)\right| / S_0$, with p_{sig} the measured pressure. (Dark blue) Estimated correction function $S^{-1}(f)$. (Solid red curve) Estimated response function using Bergh and Tijdeman (1965), $|G(i\omega)|$. (Red dashed line) Frequency of the first resonance peak.

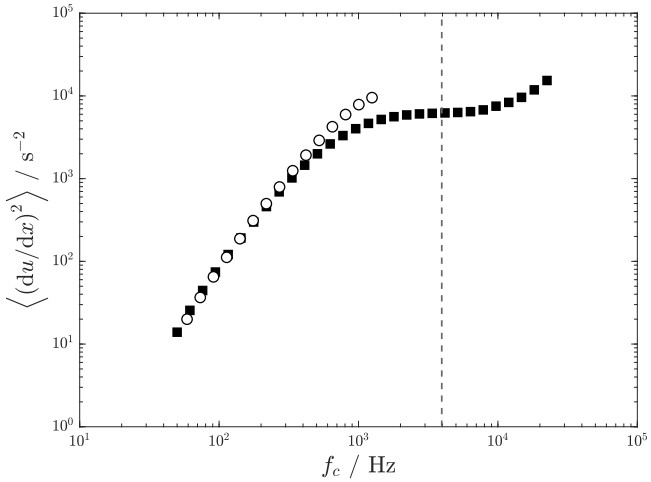

Fig. C3: Ensemble-averaged squared forward difference as a function of the cutoff frequency for the unfiltered timeseries of case B. ■: Hot-wire data; ○: Cobra data. The dashed line represents the Kolmogorov advection frequency.

presented in section 2.2). The points beyond this frequency represented noise and were removed by low-pass filtering the signal. For the Cobra probe, as observed in figure 4, the velocity gradient exceeded the HW gradient for increasing f_c. Consequently, the gradient evaluated at the highest possible frequency for the Cobra probe overestimated the gradient computed at f_K for the HW, leading to a discrepancy in the estimation of the dissipation rate with the Cobra probe.

Table C1: Turbulence dissipation scales derived from the hot-wire signal using numerical differentiation.

Grid case	λ (mm)	η (mm)	ε (m^2s^{-3})	Re_λ (−)
A	3.14	0.35	0.27	22
B	3.08	0.23	1.40	50
C	3.14	0.16	5.33	103

Schemes with a higher order of accuracy were compared. These methods smoothed the estimations by accounting for more points in a central difference, expressed as

$$\frac{\mathrm{d}u}{\mathrm{d}x} = \frac{1}{\mathrm{d}x} \sum_{k=-n}^{n} a_k u(x + k\mathrm{d}x) + \mathcal{O}\left(\mathrm{d}x^{2n}\right), \tag{C2}$$

where $2n$ represents the order of accuracy, and where the coefficients c_k are determined with

$$c_k = \frac{1!(-1)^{k+1}(n!)^2}{k(n-k)!(n+k)!}, \qquad (k \neq 0). \tag{C3}$$

In total, five centered finite-difference schemes were compared, with accuracy orders of $\mathcal{O}(\mathrm{d}x^2)$, $\mathcal{O}(\mathrm{d}x^4)$, $\mathcal{O}(\mathrm{d}x^6)$, $\mathcal{O}(\mathrm{d}x^8)$, and $\mathcal{O}(\mathrm{d}x^{10})$. These schemes used $2n+1$ points, corresponding to a total of 3, 5, 7, 9, and 11 points, respectively. The performance of these differentiation schemes is illustrated in figure C4. Figures C4(a), (c), and (e) represent data acquired with the HW. The gradients converged consistently around f_K for all schemes, with a maximum deviation below 1%. Table C1 summarizes the dissipation scales computed using numerical differentiation for the HW. This is no longer observed in the high frequencies, where the gradients started to diverge, highlighting the different sensitivity of each scheme to noise. In figures C4(b), (d), and (f), the results of the Cobra probe were compared to the averaged HW results (represented by the dotted black line). Unlike the HW results, the differentiation schemes began to diverge much earlier due to the limitations explained earlier in section 3.

The limitations inherent to the probe, together with aliasing issues, prevent convergence of the velocity gradient regardless of the accuracy order employed. This conclusion can be directly observed by comparing the values of the turbulence quantities computed from the gradients obtained with the different accuracy orders. In figure C5(a), the 4^{th}-order accuracy scheme ($n = 2$) seemed to better approximate the expected value. Gradients computed with higher accuracy orders tended to decrease with increasing FST. However, for $n = 2$, the curve aligned with this trend at lower turbulence levels but deviated once some critical turbulence was reached, suggesting that the difference might begin to increase similarly to the difference for $n = 1$ for higher FST. As the Kolmogorov scale η is essentially dependent on ν and ε, its computation is straightforward using equation 2. However, using the same velocity gradient used for the computation of ε and η for the computation of λ led to an inaccurate estimation. This scale is indeed directly proportional to the RMS of the fluctuations. Since the RMS value is overestimated due to spectral divergence, the estimation of λ and the corresponding Reynolds number, $Re_\lambda = \sqrt{\overline{u'^2}}\lambda/\nu$, were affected. This effect

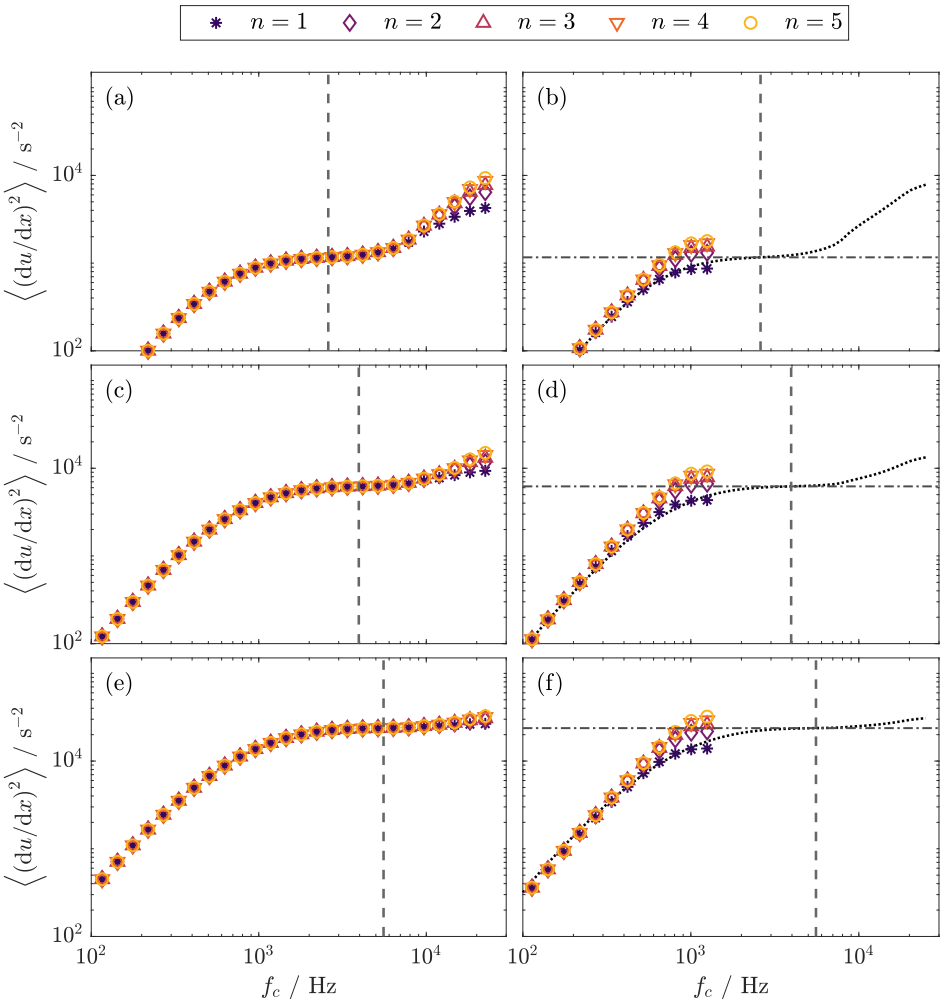

Fig. C4: Ensemble-averaged squared velocity gradient as a function of the cutoff frequency from hot-wire (a, c, e) and Cobra measurements (b, d, f). (a, b): case A; (c, d): case B; (e, f): case C; $\cdots$: Average of the different schemes from hot-wire measurements; - - -: f_K; - $\cdot$ -: Averaged-squared velocity gradient measured from hot-wire measurements at f_K.

is shown in figure C5(b) where λ ($\propto \sqrt{\overline{u'^2}}$) seemed to be closer to the HW estimation when a 6^{th}-order accuracy scheme was employed while figure C5(c) indicates that for Re_λ ($\propto \overline{u'^2}$), a 10^{th}-order accuracy scheme was required to counterbalance the overestimation on $\sqrt{\overline{u'^2}}$.

Except for certain accuracy orders that yield values comparable to those obtained with the hot-wire for specific quantities, no single order consistently reproduced reliable estimates across all turbulence statistics. This implies that different accuracy

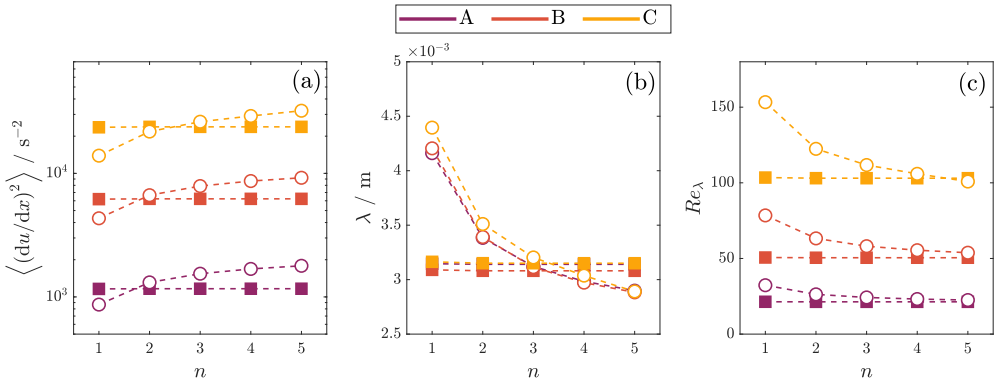

Fig. C5: (a) Ensemble-averaged squared velocity gradient versus differentiation accuracy level for each turbulent case. (b) Taylor microscale versus differentiation accuracy level for each turbulent case. (c) Reynolds number computed with λ versus differentiation accuracy level for each turbulent case. ■: Hot-wire data; ○: Cobra data.

orders would need to be employed to evaluate the velocity gradient for the estimation of different quantities, which contradicts the HIT assumptions, suggesting that λ, ε, and η are inherently linked through this velocity gradient.

References

Bodenschatz, E., Bewley, G.P., Nobach, H., Sinhuber, M., Xu, H.: Variable density turbulence tunnel facility. Review of Scientific Instruments **85**(9), 093908 (2014) https://doi.org/10.1063/1.4896138

Benedict, L.H., Gould, R.D.: Towards better uncertainty estimates for turbulence statistics. Experiments in Fluids **22**(2), 129–136 (1996) https://doi.org/10.1007/s003480050030

Bearman, P.W., Morel, T.: Effect of free stream turbulence on the flow around bluff bodies. Progress in Aerospace Sciences **20**(2), 97–123 (1983) https://doi.org/10.1016/0376-0421(83)90002-7

Bergh, H., Tijdeman, H.: Theoretical and experimental results for the dynamic response of pressure measuring systems. Technical report (nlr-tr f.238), National Aero- and Astronautical Research Institute (NLR), Amsterdam (1965). https://doi.org/10.13140/2.1.4790.1123

Bailey, S.C.C., Tavoularis, S., Lee, B.H.K.: Effects of free-stream turbulence on wingtip vortex formation and near field. Journal of Aircraft **43**(5), 1282–1291 (2006) https://doi.org/10.2514/1.19433

Comte-Bellot, G.: Hot-wire anemometry. Annual Review of Fluid Mechanics **8**, 209–231 (1976) https://doi.org/10.1146/annurev.fl.08.010176.001233

Creyssels, M., Dupont, P., Ould El Moctar, A., Valance, A., Cantat, I., Jenkins, J.T., Pasini, J.M., Rasmussen, K.R.: Saltating particles in a turbulent boundary layer: experiment and theory. Journal of Fluid Mechanics **625**, 47–74 (2009) https://doi.org/10.1017/S0022112008005491

Chen, J., Haynes, B.S., Fletcher, D.F.: Cobra Probe Measurements of Mean Velocities, Reynolds Stresses and Higher-Order Velocity Correlations in Pipe Flow. Experimental Thermal and Fluid Science **21**(4), 206–217 (2000) https://doi.org/10.1016/S0894-1777(00)00004-2

Donzis, D.A., Sreenivasan, K.R.: The bottleneck effect and the kolmogorov constant in isotropic turbulence. Journal of Fluid Mechanics **657**, 171–188 (2010) https://doi.org/10.1017/S0022112010001400

Ertunç, O., Özyilmaz, N., Lienhart, H., Durst, F., Beronov, K.: Homogeneity of turbulence generated by static-grid structures. Journal of Fluid Mechanics **654**, 473–500 (2010) https://doi.org/10.1017/S0022112010000479

Frisch, U.: Turbulence: The Legacy of A. N. Kolmogorov. Cambridge University Press, Cambridge (1995)

Hussein, H., George, W.: Influence of wire spacing on derivative measurement with parallel hot-wire probes. Forum on Turbulent Flows-1990, 121–124 (1990)

Heckmeier, F.M., Hayböck, S., Breitsamter, C.: Spatial and temporal resolution of a fast-response aerodynamic pressure probe in grid-generated turbulence. Experiments in Fluids **62**(44) (2021) https://doi.org/10.1007/s00348-021-03141-7

Hinze, J.O.: Turbulence. McGraw-Hill, Michigan (1975)

Hearst, R.J., Lavoie, P.: The effect of active grid initial conditions on high reynolds number turbulence. Experiments in Fluids **56**, 185 (2015) https://doi.org/10.1007/s00348-015-2052-1

Hooper, J., Musgrove, A.: Reynolds stress, mean velocity, and dynamic static pressure measurement by a four-hole pressure probe. Experimental thermal and fluid science **15**(4), 375–383 (1997)

Irwin, H.P.A.H., Cooper, K.R., Girard, R.: Correction of distortion effects caused by tubing systems in measurements of fluctuating pressures. Journal of Wind Engineering and Industrial Aerodynamics **5**(1), 93–107 (1979) https://doi.org/10.1016/0167-6105(79)90026-6

Isaza, J., Salazar, R., Warhaft, Z.: On grid-generated turbulence in the near- and far field regions. Journal of Fluid Mechanics **753**, 402–426 (2014) https://doi.org/10.1017/jfm.2014.375

Jørgensen, F.E.: How to measure turbulence with hot-wire anemometers: a practical guide. Dantec dynamics (2001)

Kovaerk, M., Amatucci, L., Gillis, K.A., Potra, F., Ratino, J., Levitan, M.L., Yeo, D.: Calibration of dynamic pressure in a tubing system and optimized design of tube configuration: A numerical and experimental study (2018)

Kurian, T., Fransson, J.H.M.: Grid-generated turbulence revisited. Fluid Dynamics Research **41**(2), 021403 (2009) https://doi.org/10.1088/0169-5983/41/2/021403

Kolmogorov, A.N.: Dissipation of Energy in the Locally Isotropic Turbulence. Dokl. Akad. Nauk SSSR **32**(16) (1941)

Laneville, A.: Effects of turbulence on wind induced vibrations of bluff cylinders. PhD thesis, University of British Columbia (1973). https://doi.org/10.14288/1.0101058

Larssen, J.V., Devenport, W.J.: On the generation of large-scale homogeneous turbulence. Experiments in Fluids **50**, 1207–1223 (2011) https://doi.org/10.1007/s00348-010-0974-1

Lee, B.E.: Some effects of turbulence scale on the mean forces on a bluff body. Journal of Wind Engineering and Industrial Aerodynamics **1**, 361–370 (1975) https://doi.org/10.1016/0167-6105(75)90030-6

Lohse, D., Müller-Groeling, A.: Bottleneck effects in turbulence: Scaling phenomena in r versus p space. Phys. Rev. Lett. **74**, 1747–1750 (1995) https://doi.org/10.1103/PhysRevLett.74.1747

Lohse, D.: Crossover from high to low reynolds number turbulence. Phys. Rev. Lett. **73**, 3223–3226 (1994) https://doi.org/10.1103/PhysRevLett.73.3223

Mauro, S., Lanzafame, R., Messina, M., Brusca, S., Famoso, F., Galvagno, A.: Small-scale open-circuit wind tunnel: Design criteria, construction and calibration. International Journal of Applied Engineering Research **12**, 13649–13662 (2017)

Moss, R.W., Oldfield, M.L.G.: Comparisons between turbulence spectra measured with fast response pressure transducers and hot wires. In: Proceedings of 10th Symposium VKI (1990)

Mydlarski, L., Warhaft, Z.: On the onset of high-reynolds-number grid-generated wind tunnel turbulence. Journal of Fluid Mechanics **320**, 331–368 (1996) https://doi.org/10.1017/S0022112096007562

Nedić, J., Tavoularis, S., Marusic, I.: Dissipation scaling in constant-pressure turbulent boundary layers. Phys. Rev. Fluids **2**, 032601 (2017) https://doi.org/10.1103/PhysRevFluids.2.032601

Obligado, M., Brun, C., Silvestrini, J., Camano Schettini, E.: Dissipation Scalings in

the Turbulent Boundary Layer at Moderate Re_θ. Flow, Turbulence and Combustion **108** (2022) https://doi.org/10.1007/s10494-021-00270-1

Pearson, B.R., Krogstad, P.-A., Water, W.: Measurements of the turbulent energy dissipation rate. Physics of Fluids **14**(3), 1288–1290 (2002) https://doi.org/10.1063/1.1445422

Roach, P.E.: The generation of nearly isotropic turbulence by means of grids. International Journal of Heat and Fluid Flow **8**(2), 82–92 (1987) https://doi.org/10.1016/0142-727X(87)90001-4

Sumer, B.M., Chua, L.H.C., Cheng, N.-S., Fredsøe, J.: Influence of turbulence on bed load sediment transport. Journal of Hydraulic Engineering **129**(8), 585–596 (2003) https://doi.org/10.1061/(ASCE)0733-9429(2003)129:8(585)

Shepherd, I.C.: A four hole pressure probe for fluid flow measurements in three dimensions. J. Fluids. Eng. **103**, 590–594 (1981) https://doi.org/10.1115/1.3241774

Sreenivasan, K.R.: On the scaling of the turbulence energy dissipation rate. The Physics of Fluids **27**(5), 1048–1051 (1984) https://doi.org/10.1063/1.864731 https://pubs.aip.org/aip/pfl/article-pdf/27/5/1048/12367752/1048_1_online.pdf

Sreenivasan, K.R.: On the universality of the kolmogorov constant. Physics of Fluids **7**(11), 2778–2784 (1995) https://doi.org/10.1063/1.868656

Saddoughi, S.G., Veeravalli, S.V.: Local isotropy in turbulent boundary layers at high reynolds number. Journal of Fluid Mechanics **268**, 333–372 (1994) https://doi.org/10.1017/S0022112094001370

Su, H., Yang, Y., Pope, S.B.: Simple model for the bottleneck effect in isotropic turbulence based on kolmogorov's hypotheses. Phys. Rev. Fluids **8**, 014603 (2023) https://doi.org/10.1103/PhysRevFluids.8.014603

Taylor, G.I.: Statistical theory of turbulence. Proceedings of the Royal Society of London. Series A - Mathematical and Physical Sciences **151**(873), 421–444 (1935) https://doi.org/10.1098/rspa.1935.0158

Taylor, G.I.: The Spectrum of Turbulence. Proceedings of the Royal Society of London. Series A - Mathematical and Physical Sciences **164**(919), 476–490 (1938) https://doi.org/10.1098/rspa.1938.0032

Turbulent Flow Instrumentation: Cobra Probe references. https://www.turbulentflow.com.au/Products/CobraProbe/CobraReferences.php. Accessed: 2025-09-04

Verma, M.K., Donzis, D.: Energy transfer and bottleneck effect in turbulence. Journal of Physics A: Mathematical and Theoretical **40**(16), 4401 (2007) https://doi.org/10.1088/1751-8113/40/16/010

Vita, G., Hemida, H., Andrianne, T., Baniotopoulos, C.C.: Generating atmospheric turbulence using passive grids in an expansion test section of a wind tunnel. Journal of Wind Engineering and Industrial Aerodynamics **178**, 91–104 (2018) https://doi.org/10.1016/j.jweia.2018.02.007

Valance, A., Rasmussen, K.R., Ould El Moctar, A., Dupont, P.: The Physics of Aeolian Sand Transport. Comptes Rendus Physique **16**(1), 105–117 (2015)

Watkins, S., Ravi, S., Loxton, B.: The effect of turbulence on the aerodynamics of low reynolds number wings. Engineering Letters **18** (2010)

Wyngaard, J.C.: Spatial resolution of the vorticity meter and other hot-wire arrays. Journal of Physics E: Scientific Instruments **2**(11), 983 (1969) https://doi.org/10.1088/0022-3735/2/11/320

Zheng, Y., Nakamura, K., Nagata, K., Watanabe, T.: Unsteady dissipation scaling in static- and active-grid turbulence. Journal of Fluid Mechanics **956**, 20 (2023) https://doi.org/10.1017/jfm.2022.937